

Fast Generation of Pipek–Mezey Wannier Functions via the Co-Iterative Augmented Hessian Method

Gengzhi Yang^{1,2} and Hong-Zhou Ye^{3,4, a)}

¹⁾*Joint Center for Quantum Information and Computer Science, University of Maryland, College Park, Maryland, 20742*

²⁾*Department of Mathematics, University of Maryland, College Park, Maryland, 20742*

³⁾*Department of Chemistry and Biochemistry, University of Maryland, College Park, Maryland, 20742*

⁴⁾*Institute for Physical Science and Technology, University of Maryland, College Park, Maryland, 20742*

(Dated: 16 February 2026)

We report a k -point extension of the second-order co-iterative augmented Hessian (CIAH) algorithm, termed k -CIAH, for Pipek–Mezey (PM) localization of Wannier functions (WFs). By exploiting an efficient evaluation of the Hessian–vector product, k -CIAH achieves $O(N_k^2 n^3)$ scaling in both CPU time and memory, matching that of previously reported first-order k -space approaches while improving upon the $O(N_k^3 n^3)$ scaling of Γ -point CIAH, where N_k denotes the number of k -points sampling the first Brillouin zone and n characterizes the unit-cell size. Benchmark calculations on a diverse set of solids—including insulators, semiconductors, metals, and surfaces—demonstrate the fast and robust convergence of k -CIAH-based PMWF optimization, which yields an overall computational efficiency approximately 2–3-fold higher than first-order k -space methods and orders of magnitude higher than Γ -point CIAH for localizing 1000–5000 orbitals. The quality of the resulting PMWFs is further validated by accurate electronic band structures obtained via PMWF-based Wannier interpolation.

I. INTRODUCTION

Wannier functions^{1,2} (WFs) provide a localized real-space representation of Bloch orbitals and underpin a wide range of important applications, including band interpolation,^{3,4} evaluation of response properties,⁵ Hamiltonian downfolding,^{6–10} construction of machine-learning interatomic potentials,^{11–13} and reduced-scaling many-body methods based on quantum embedding^{14–18} and local correlation theories,^{19–25} among others. Several localization criteria have been developed, most prominently the Foster–Boys scheme²⁶ (commonly referred to as maximally localized WFs^{27–29} in the physics and materials science communities), the fourth-moment scheme,³⁰ the Edmiston–Ruedenberg scheme,³¹ and the Pipek–Mezey (PM) scheme,³² which differ in how localization is quantified.

Among these, PM localization is particularly attractive for periodic systems because it is formulated in terms of atomic populations, whose definition is straightforward under periodic boundary conditions, and yields chemically intuitive orbitals that preserve σ and π symmetry.³² The original PM formulation relies on Mulliken atomic populations,³² which are ill-defined in large basis sets with polarization and diffuse functions. This limitation has been largely overcome by the development of more robust population schemes, including meta-Löwdin,³³ projection onto intrinsic atomic orbitals³⁴ or auxiliary minimal bases,³⁵ and various real-space density partitioning approaches,³⁶ thereby rendering PM-based localization reliable for calculations employing high-quality basis sets.^{22–24,36}

For periodic systems sampled with a uniform k -mesh, recent work has established gradient-based PMWF optimiza-

tion in reciprocal space,^{35,37,38} most notably through k -point implementations of the Broyden–Fletcher–Goldfarb–Shanno (BFGS) algorithm,^{39–42} which exhibit improved convergence compared to steepest-ascent or conjugate-gradient methods. These approaches generate PMWFs that preserve translational symmetry and avoid the cubic scaling of supercell-based Γ -point formulations, thereby enabling localization for increasingly large k -meshes and complex materials. Nevertheless, their performance remains limited by the intrinsic first-order convergence of quasi-Newton methods.

In this work, we introduce a second-order strategy for PMWF generation based on the co-iterative augmented Hessian⁴³ (CIAH) method. Originally developed for molecular orbital optimization,^{43,44} CIAH has been successfully applied to Γ -point supercell calculations in periodic solids.^{22–24,45} Here we generalize this framework to Bloch orbitals with k -point sampling, yielding what we term the k -CIAH method. By exploiting an efficient evaluation of the Hessian–vector product, k -CIAH achieves $O(N_k^2 n^3)$ scaling in both CPU time and memory, rivaling first-order k -space methods while retaining the quadratic convergence characteristic of molecular and Γ -point CIAH. Benchmark calculations on a diverse set of solids—including insulators, semiconductors, metals, and surfaces—demonstrate the fast and robust convergence of k -CIAH, resulting in overall computational efficiencies approximately 2–3 times higher than the k -space BFGS algorithm and orders of magnitude higher than Γ -point CIAH when localizing 1000–5000 orbitals. The quality of the resulting PMWFs is further validated by accurate electronic band structures obtained via PMWF-based Wannier interpolation.^{4,29}

The rest of this paper is organized as follows. In section II, we present the theoretical framework of k -CIAH and its efficient implementation. Section III describes computational details. Numerical benchmarks, including convergence behavior

^{a)}Electronic mail: hzye@umd.edu

(section IV A), cost analysis (section IV B), and Wannier interpolation (section IV C), are reported in section IV, followed by concluding remarks in section V.

II. THEORY

A. Notations

Throughout this paper, we consider a uniform k -point mesh \mathcal{K} of size N_k sampling the first Brillouin zone and n_{orb} Bloch orbitals $\{\phi_{\mathbf{k}i}\}$ per k -point to be localized. Let $\mathbf{R} \in \mathcal{L}$ label the N_k unit cells in the Born–von Kármán (BvK) supercell associated with \mathcal{K} . The Bloch orbitals can be transformed into an equal number of Wannier functions (WFs) in the BvK supercell via

$$w_{\mathbf{R}i}(\mathbf{r}) = \sum_{\mathbf{k}}^{N_k} \phi_{\mathbf{k}i}(\mathbf{r}) \theta_{\mathbf{R}k}^*, \quad (1)$$

where $\theta_{\mathbf{R}k} = (1/\sqrt{N_k}) e^{i\mathbf{R}\cdot\mathbf{k}}$. By construction, WFs in different unit cells are related by lattice translation,

$$w_{\mathbf{R}i}(\mathbf{r}) = w_{\mathbf{0}i}(\mathbf{r} - \mathbf{R}). \quad (2)$$

Each unit cell contains n_{atom} atoms and n_{proj} atom-centered projectors $\{\chi_{\mathbf{k}\mu}\}$ per k -point, which are likewise Bloch functions. The corresponding Wannier-transformed projectors are defined analogously as

$$\chi_{\mathbf{R}\mu}(\mathbf{r}) = \sum_{\mathbf{k}}^{N_k} \chi_{\mathbf{k}\mu}(\mathbf{r}) \theta_{\mathbf{R}k}^*, \quad (3)$$

and are used to define the atomic populations entering the PM localization scheme described in section II B. The size of the atomic projector basis depends on the projector type and typically ranges from that of a minimal basis to that of the full atomic-orbital basis. We note that $n_{\text{proj}} \geq n_{\text{orb}}$ is a necessary condition for obtaining well-defined atomic populations in eq. (5).

Within the BvK supercell, we denote the total numbers of atoms, atomic projectors, and orbitals to be localized by N_{atom} , N_{proj} , and N_{orb} , respectively; these are related to their per-cell or per- k -point counterparts by a factor of N_k (e.g., $N_{\text{orb}} = N_k n_{\text{orb}}$). When analyzing computational scaling in section II E, we also use n as a generic symbol for quantities that scale only with the unit-cell size (such as n_{orb} , n_{atom} , and n_{proj}).

B. Pipek–Mezey Wannier functions (PMWFs)

The PMWFs are defined as WFs that maximize the PM objective function,

$$L_p = \sum_{\mathbf{T}A}^{N_{\text{atom}}} \sum_i^{n_{\text{orb}}} Q_{\mathbf{T}A,0i}^p, \quad (4)$$

where $Q_{\mathbf{T}A,\mathbf{R}i}$ denotes the atomic population of the WF $w_{\mathbf{R}i}$ on atom A in cell \mathbf{T} ,

$$Q_{\mathbf{T}A,\mathbf{R}i} = \langle w_{\mathbf{R}i} | \hat{P}_{\mathbf{T}A} | w_{\mathbf{R}i} \rangle, \quad (5)$$

and $p \geq 2$ is a positive integer. Exploiting the translational invariance of the WFs in eq. (2), we include in eq. (4) only the populations of WFs in a reference cell (taken as $\mathbf{R} = \mathbf{0}$).

The atomic projection operator $\hat{P}_{\mathbf{T}A}$ is constructed from the Wannier-transformed projectors in eq. (3). For orthonormal projectors,

$$\hat{P}_{\mathbf{T}A} = \sum_{\mu \in A} |\chi_{\mathbf{T}\mu}\rangle \langle \chi_{\mathbf{T}\mu}|, \quad (6)$$

whereas for non-orthogonal projectors we use the symmetrized form

$$\hat{P}_{\mathbf{T}A} = \frac{1}{2} \sum_{\mu \in A} \left(|\chi_{\mathbf{T}\mu}\rangle \langle \tilde{\chi}_{\mathbf{T}\mu}| + |\tilde{\chi}_{\mathbf{T}\mu}\rangle \langle \chi_{\mathbf{T}\mu}| \right), \quad (7)$$

where

$$\tilde{\chi}_{\mathbf{T}\mu}(\mathbf{r}) = \sum_{\mathbf{S}\nu}^{N_{\text{atom}}} \chi_{\mathbf{S}\nu}(\mathbf{r}) (S^{-1})_{\mathbf{S}\nu, \mathbf{T}\mu} \quad (8)$$

are biorthogonal to $\chi_{\mathbf{T}\mu}$, with $S_{\mathbf{S}\mu, \mathbf{T}\nu} = \langle \chi_{\mathbf{S}\mu} | \chi_{\mathbf{T}\nu} \rangle$. The definitions in eqs. (6) and (7) ensure that $\hat{P}_{\mathbf{T}A}$ is Hermitian, which in turn guarantees that $Q_{\mathbf{T}A,\mathbf{R}i}$ and the PM objective in eq. (4) are real-valued even for complex WFs.

The PM objective function is invariant under a translationally invariant (i.e., \mathbf{R} -independent) gauge transformation of the WFs,

$$w_{\mathbf{R}i}(\mathbf{r}) \rightarrow e^{i\eta_i} w_{\mathbf{R}i}(\mathbf{r}), \quad \forall \mathbf{R} \in \mathcal{L}. \quad (9)$$

In reciprocal space, eq. (9) corresponds to a k -independent phase transformation of the Bloch orbitals,

$$\phi_{\mathbf{k}i}(\mathbf{r}) \rightarrow e^{i\eta_i} \phi_{\mathbf{k}i}(\mathbf{r}), \quad \forall \mathbf{k} \in \mathcal{K}. \quad (10)$$

As discussed in section II C, fixing these gauge degrees of freedom reduces the number of independent parameters in the PMWF parameterization.

C. Parameterization of PMWFs

In this work, we parameterize the PMWFs in reciprocal space by applying unitary rotations to an initial set of Bloch orbitals $\{\phi_{\mathbf{k}i}^{(0)}\}$ (e.g., selected crystalline orbitals from a mean-field calculation),

$$w_{\mathbf{R}i}(\mathbf{r}) = \sum_{\mathbf{k}}^{N_k} \left[\sum_j^{n_{\text{orb}}} \phi_{\mathbf{k}j}^{(0)}(\mathbf{r}) U_{\mathbf{k},ji} \right] \theta_{\mathbf{R}k}^*. \quad (11)$$

Equation (11) is equivalent to a real-space formulation in which a single, translationally invariant unitary transformation is applied to the initial WFs $\{w_{\mathbf{R}i}^{(0)}\}$ associated with $\{\phi_{\mathbf{k}i}^{(0)}\}$,

$$w_{\mathbf{R}i}(\mathbf{r}) = \sum_{\mathbf{S}j}^{N_{\text{orb}}} w_{\mathbf{S}j}^{(0)}(\mathbf{r}) U_{\mathbf{S}j, \mathbf{R}i}. \quad (12)$$

The reciprocal- and real-space unitaries are connected by a double Fourier transform,

$$U_{\mathbf{S}j,\mathbf{R}i} = \sum_{\mathbf{k}} \theta_{\mathbf{S}\mathbf{k}} U_{\mathbf{k},ji} \theta_{\mathbf{R}\mathbf{k}}^*, \quad (13)$$

from which it follows that the real-space unitary is translationally invariant,

$$U_{\mathbf{S}j,\mathbf{R}i} = U_{\mathbf{0}j,(\mathbf{R}-\mathbf{S})i}. \quad (14)$$

We parameterize each of the N_k reciprocal-space unitary matrices in exponential form,

$$U_{\mathbf{k}} = e^{\kappa_{\mathbf{k}}}, \quad (15)$$

where the generators $\{\kappa_{\mathbf{k}}\}$ are anti-Hermitian,

$$\kappa_{\mathbf{k}} = -\kappa_{\mathbf{k}}^\dagger, \quad (16)$$

so that $U_{\mathbf{k}}$ is unitary by construction. Each $\kappa_{\mathbf{k}}$ contains n_{orb}^2 real degrees of freedom. Writing $\kappa_{\mathbf{k}} = X_{\mathbf{k}} + iY_{\mathbf{k}}$ with real matrices $X_{\mathbf{k}}$ and $Y_{\mathbf{k}}$, a convenient choice of independent parameters is given by (i) the lower-triangular part of the antisymmetric matrix $X_{\mathbf{k}}$ (excluding the diagonal) and (ii) the lower-triangular part of the symmetric matrix $Y_{\mathbf{k}}$ (including the diagonal).

To fix the gauge freedom identified in eq. (10), we set $\text{diag}(\kappa_{\mathbf{k}}) = i \text{diag}(Y_{\mathbf{k}})$ to zero for one chosen k -point. The total number of independent real parameters is therefore $N_k n_{\text{orb}}^2 - n_{\text{orb}}$. These parameters generate N_k independent complex unitaries $\{U_{\mathbf{k}}\}$, which correspond via eq. (13) to a single complex, translationally invariant real-space unitary acting on the supercell WFs. The special case in which this real-space unitary is constrained to be real-valued is discussed in section II G.

D. Optimization of PMWFs using the co-iterative augmented Hessian (CIAH) method

In this work, we determine the unitary rotations that transform the initial Bloch orbitals into the final PMWFs in eq. (11) using the second-order co-iterative augmented Hessian (CIAH) algorithm.⁴³ CIAH is a modified trust-region Newton method⁴⁶ that has been successfully applied to orbital localization in molecules^{43,44} and in periodic solids with Γ -point Brillouin zone sampling.^{22–24,45} Near a local minimum, CIAH exhibits quadratic convergence while maintaining sufficient descent away from convergence.⁴³ In this section, we extend the molecular and Γ -point formulations of CIAH to general Bloch orbitals; we refer to this generalization as k -CIAH.

Starting from an initial guess $\{U_{\mathbf{k}}^{(0)}\}$ (see section II F), k -CIAH updates the k -space unitary rotations directly at each iteration,

$$U_{\mathbf{k}}^{(n+1)} = U_{\mathbf{k}}^{(n)} e^{\kappa_{\mathbf{k}}^{(n+1)}}, \quad (17)$$

where the step in generator space $\{\kappa_{\mathbf{k}}^{(n+1)}\}$ is obtained by solving an augmented Hessian eigenvalue problem with the Davidson algorithm.⁴⁷

$$\begin{bmatrix} 0 & \mathbf{g}^{(n)\dagger} \\ \mathbf{g}^{(n)} & \mathbf{H}^{(n)} \end{bmatrix} \begin{bmatrix} 1 \\ \mathbf{x}^{(n+1)} \end{bmatrix} = \epsilon \begin{bmatrix} 1 \\ \mathbf{x}^{(n+1)} \end{bmatrix}. \quad (18)$$

Here, $\mathbf{x}^{(n+1)}$ collects the independent real parameters in the generators $\{\kappa_{\mathbf{k}}^{(n+1)}\}$. $\mathbf{g}^{(n)}$ and $\mathbf{H}^{(n)}$ denote the gradient and Hessian of the negative PM objective in eq. (4), evaluated at the current orbitals and at zero generator,

$$\begin{aligned} g_{\alpha}^{(n)} &= -\left. \frac{\partial L_p^{(n)}}{\partial x_{\alpha}} \right|_{\mathbf{x}=\mathbf{0}}, \\ H_{\alpha\beta}^{(n)} &= -\left. \frac{\partial^2 L_p^{(n)}}{\partial x_{\alpha} \partial x_{\beta}} \right|_{\mathbf{x}=\mathbf{0}}, \end{aligned} \quad (19)$$

with $L_p^{(n)} = L_p[\{U_{\mathbf{k}}^{(n)}\}]$.

The analytical gradient, Hessian–vector product, and Hessian diagonal elements required to solve eq. (18) with the Davidson algorithm are derived in the Supporting Information. (The Hessian diagonals are used to precondition the Davidson update.⁴⁷) We summarize the working equations below.

We first define two types of matrix elements of the atomic projection operators,

$$\begin{aligned} (P_{\mathbf{T}A,\mathbf{kk}'})_{ij} &= \frac{1}{N_k} \langle \phi_{\mathbf{k}i} | \hat{P}_{\mathbf{T}A} | \phi_{\mathbf{k}'j} \rangle = \frac{1}{N_k} \sum_{\mu \in A} O_{\mathbf{T}\mu,\mathbf{k}i}^* O_{\mathbf{T}\mu,\mathbf{k}'j}, \\ (P_{\mathbf{T}A,\mathbf{k}0})_{ij} &= \frac{1}{\sqrt{N_k}} \langle \phi_{\mathbf{k}j} | \hat{P}_{\mathbf{T}A} | w_{\mathbf{0}i} \rangle = \frac{1}{\sqrt{N_k}} \sum_{\mu \in A} O_{\mathbf{T}\mu,\mathbf{k}i}^* O_{\mathbf{T}\mu,\mathbf{0}j}, \end{aligned} \quad (20)$$

where

$$\begin{aligned} O_{\mathbf{T}\mu,\mathbf{k}i} &= \langle \chi_{\mathbf{T}\mu} | \phi_{\mathbf{k}i} \rangle, \\ O_{\mathbf{T}\mu,\mathbf{0}i} &= \langle \chi_{\mathbf{T}\mu} | w_{\mathbf{0}i} \rangle, \end{aligned} \quad (21)$$

are overlaps between atomic projectors and Bloch orbitals (or WFs). At each k -point, the gradient corresponds to the lower-triangular part of the anti-Hermitian matrix

$$G_{\mathbf{k}ij} = f_{ij} \hat{A}_{ij} \left\{ -2p \sum_{\mathbf{T}A}^{N_{\text{atom}}} Q_{\mathbf{T}A,\mathbf{0}j}^{p-1} (P_{\mathbf{T}A,\mathbf{k}0})_{ij} \right\}, \quad (22)$$

where $f_{ij} = 1 - \delta_{ij}/2$ and $\hat{A}_{ij} B_{kij} = (\mathbf{B}_{\mathbf{k}} - \mathbf{B}_{\mathbf{k}}^\dagger)_{ij}$. Similarly, the Hessian–vector product at each k -point is given by the lower-triangular part of

$$(\mathbf{Hv})_{\mathbf{k}ij} = f_{ij} \hat{A}_{ij} \left\{ \tilde{\sigma}_{\mathbf{k}ij}^{\text{d}} + \tilde{\sigma}_{\mathbf{k}ij}^{\text{c-symm}} + \tilde{\sigma}_{\mathbf{k}ij}^{\text{c-asymm}} \right\}, \quad (23)$$

with

$$\tilde{\sigma}_{\mathbf{k}ij}^{\text{d}} = -4p(p-1) \sum_{\mathbf{T}A}^{N_{\text{atom}}} Q_{\mathbf{T}A,\mathbf{0}j}^{p-2} \sum_{\mathbf{k}'}^{N_k} \Re \left[(v_{\mathbf{k}'}^\dagger P_{\mathbf{T}A,\mathbf{k}'\mathbf{0}})_{jj} \right] (P_{\mathbf{T}A,\mathbf{k}0})_{ij}, \quad (24)$$

$$\tilde{\sigma}_{\mathbf{k}ij}^{\text{c-symm}} = -2p \sum_{\mathbf{T}A}^{N_{\text{atom}}} Q_{\mathbf{T}A,0j}^{p-1} \sum_{\mathbf{k}'}^{N_k} (P_{\mathbf{T}A,\mathbf{k}\mathbf{k}'} v_{\mathbf{k}'})_{ij}, \quad (25)$$

$$\begin{aligned} \tilde{\sigma}_{\mathbf{k}ij}^{\text{c-asymm}} &= -p \sum_m^{n_{\text{orb}}} \left[\sum_{\mathbf{T}A}^{N_{\text{atom}}} Q_{\mathbf{T}A,0m}^{p-1} (P_{\mathbf{T}A,\mathbf{k}\mathbf{0}})_{im} \right] v_{\mathbf{k}jm}^* \\ &\quad - p \sum_{\mathbf{T}A}^{N_{\text{atom}}} Q_{\mathbf{T}A,0j}^{p-1} (v_{\mathbf{k}}^\dagger P_{\mathbf{T}A,\mathbf{k}\mathbf{0}})_{ij}. \end{aligned} \quad (26)$$

These correspond to the disconnected, connected symmetric, and connected asymmetric contributions to the Hessian. Finally, the Hessian diagonal elements at each k -point are given by the lower-triangular part of the symmetric matrix

$$D_{\mathbf{k}ij} = f_{ij} (\tilde{D}_{\mathbf{k}ij} + \tilde{D}_{\mathbf{k}ji}), \quad (27)$$

where the real and imaginary parts of $\tilde{\mathbf{D}}_k$ read

$$\begin{aligned} (\Re \tilde{\mathbf{D}}_k)_{ij} &= -4p(p-1) \sum_{\mathbf{T}A}^{N_{\text{atom}}} Q_{\mathbf{T}A,0j}^{p-2} [(\Re P_{\mathbf{T}A,\mathbf{k}\mathbf{0}})_{ij}]^2 \\ &\quad + 2p \sum_{\mathbf{T}A}^{N_{\text{atom}}} Q_{\mathbf{T}A,0i}^{p-1} \Re [(P_{\mathbf{T}A,\mathbf{k}\mathbf{0}})_{ii} - (P_{\mathbf{T}A,\mathbf{k}\mathbf{k}})_{jj}], \\ (\Im \tilde{\mathbf{D}}_k)_{ij} &= -4p(p-1) \sum_{\mathbf{T}A}^{N_{\text{atom}}} Q_{\mathbf{T}A,0j}^{p-2} [(\Im P_{\mathbf{T}A,\mathbf{k}\mathbf{0}})_{ij}]^2 \\ &\quad + 2p \sum_{\mathbf{T}A}^{N_{\text{atom}}} Q_{\mathbf{T}A,0i}^{p-1} \Re [(P_{\mathbf{T}A,\mathbf{k}\mathbf{0}})_{ii} - (P_{\mathbf{T}A,\mathbf{k}\mathbf{k}})_{jj}]. \end{aligned} \quad (28)$$

We note that the analytical gradient in eq. (22) also enables PMWF optimization using gradient-based methods, such as the BFGS quasi-Newton algorithm,^{39–42} as explored in previous studies.^{35,38} In section IV, we compare the performance and computational efficiency of k -CIAH- and k -BFGS-based PMWF optimization.

E. Cost of k -CIAH-based PMWF optimization

The computational cost of k -CIAH-based PMWF optimization is dominated by repeated evaluations of the gradient in eq. (22) and the Hessian–vector product in eq. (23) when solving the augmented Hessian eigenvalue problem in eq. (18) with the Davidson algorithm. The cost of the gradient evaluation—and therefore of gradient-based methods such as k -BFGS^{35,38}—is controlled by the construction of the projection matrix $(P_{\mathbf{T}A,\mathbf{k}\mathbf{0}})_{ij}$ via eq. (20), which requires $O(N_k^2 n_{\text{proj}} n_{\text{orb}}^2) \sim O(N_k^2 n^3)$ CPU time and the same order of memory to store the overlap matrix $O_{\mathbf{T}A,\mathbf{k}\mathbf{i}}$ in eq. (21). Below, we outline an efficient implementation of the Hessian–vector product that achieves the same asymptotic scaling in both CPU time and memory. Combined with the faster convergence of k -CIAH relative to gradient-based schemes such as k -BFGS, this $O(N_k^2 n^3)$ scaling makes k -CIAH-based PMWF optimization computationally favorable in practice (see section IV B).

1. **Connected symmetric term.** The connected symmetric contribution in eq. (25) can be assembled at $O(N_k^2 n_{\text{atom}} n_{\text{orb}}^2)$ CPU cost once the projection–vector product

$$(Pv)_{\mathbf{T}A,\mathbf{k}ij} = \sum_{\mathbf{k}'}^{N_k} \sum_m^{n_{\text{orb}}} (P_{\mathbf{T}A,\mathbf{k}\mathbf{k}'})_{im} v_{\mathbf{k}'mj} \quad (29)$$

is available. Equation (29) can itself be evaluated at $O(N_k^2 n_{\text{proj}} n_{\text{orb}}^2)$ by exploiting the factorized form of the projection operators in eqs. (6) and (7). For orthonormal projectors,

$$(Pv)_{\mathbf{T}A,\mathbf{k}ij} = \sum_{\mu \in A} O_{\mathbf{T}\mu,\mathbf{k}i}^* \left(\sum_{\mathbf{k}'}^{N_k} \sum_m^{n_{\text{orb}}} O_{\mathbf{T}\mu,\mathbf{k}'m} v_{\mathbf{k}'mj} \right), \quad (30)$$

with analogous expressions for biorthogonalized projectors. We emphasize that evaluating $(Pv)_{\mathbf{T}A,\mathbf{k}ij}$ via eq. (30) avoids the unfavorable $O(N_k^3 n^3)$ memory cost associated with explicitly storing the full projection matrix $(P_{\mathbf{T}A,\mathbf{k}\mathbf{k}'})_{ij}$, and thus constitutes a key performance optimization of the present implementation.

2. **Disconnected term.** The disconnected contribution in eq. (24) can also be constructed at $O(N_k^2 n_{\text{atom}} n_{\text{orb}}^2)$ CPU cost once the second term is evaluated efficiently using the precomputed projection–vector product in eq. (30),

$$\sum_{\mathbf{k}'}^{N_k} \Re [(v_{\mathbf{k}'}^\dagger P_{\mathbf{T}A,\mathbf{k}'\mathbf{0}})_{jj}] = \sum_{\mathbf{k}}^{N_k} (Pv)_{\mathbf{T}A,\mathbf{k}jj}. \quad (31)$$

3. **Connected asymmetric term.** The connected asymmetric part in eq. (26) can be evaluated at $O(N_k n_{\text{orb}}^3)$ cost as

$$\tilde{\sigma}_{\mathbf{k}ij}^{\text{c-asymm}} = -p \sum_m^{n_{\text{orb}}} \left(A_{\mathbf{k}im} v_{\mathbf{k}jm}^* + v_{\mathbf{k}mi}^* A_{\mathbf{k}mj} \right), \quad (32)$$

with intermediates

$$A_{\mathbf{k}ij} = \sum_{\mathbf{T}A}^{N_{\text{atom}}} Q_{\mathbf{T}A,0j} (P_{\mathbf{T}A,\mathbf{k}\mathbf{0}})_{ij}, \quad (33)$$

which can be formed at $O(N_k^2 n_{\text{atom}} n_{\text{orb}}^2)$ CPU cost.

As in the gradient evaluation, the memory footprint of the Hessian–vector product is dominated by storing the overlap matrix between atomic projectors and Bloch orbitals, $O_{\mathbf{T}\mu,\mathbf{k}i}$, whose size scales as $O(N_k^2 n_{\text{proj}} n_{\text{orb}}) \sim O(N_k^2 n^3)$.

In passing, we note that a real-space formulation based on a supercell unitary rotation in eq. (13) can in principle achieve the same $O(N_k^2 n^3)$ scaling, provided that the translational invariance of the unitary in eq. (14) is explicitly enforced in the implementation. This is not the case, however, when one directly applies a molecular PM localization code to the BvK supercell, as in previous studies.^{22–24,45} In that setting, neglecting translational symmetry may break the translational structure of the initial Bloch orbitals (or WFs) and also increases the formal scaling to $O(N_k^3 n^3)$ in both CPU time and memory, making it computationally less favorable than the k -space approach developed here. We compare the two approaches numerically in section IV.

F. Initial guess

We construct the initial guess $\{U_{\mathbf{k}}^{(0)}\}$ for PMWF optimization in two steps. First, an initial unitary $U_{\mathbf{k}_0}^{(0)}$ is obtained for a selected k -point \mathbf{k}_0 using either Cholesky decomposition⁴⁸ or an “atomic” projection guess,⁴³ in which a set of projected atomic orbitals is constructed within the target subspace and used to initialize the localization;⁴⁹ the latter is the default initialization strategy in the PYSCF code^{50,51} for molecular orbital localization. Second, for all $\mathbf{k} \neq \mathbf{k}_0$, we align the phase of the Bloch orbitals at \mathbf{k} with those at \mathbf{k}_0 by setting

$$U_{\mathbf{k}}^{(0)} = L_{\mathbf{k}} R_{\mathbf{k}}^{\dagger}, \quad (34)$$

where $L_{\mathbf{k}}$ and $R_{\mathbf{k}}$ are the left and right singular vectors from the singular value decomposition of

$$C_{\mathbf{k}}^{\dagger} C_{\mathbf{k}_0} U_{\mathbf{k}_0}^{(0)}, \quad (35)$$

with $C_{\mathbf{k}}$ the atomic-orbital coefficient matrix of $\{\phi_{\mathbf{k}i}^{(0)}\}$. As noted in prior work,^{35,38} the construction in eqs. (34) and (35) fixes the arbitrary gauge of the initial Bloch orbitals by aligning their phases to those at \mathbf{k}_0 , which typically yields initial WFs that are primarily localized within each unit cell.

G. Real rotations

In the special case where the k -point mesh \mathcal{K} is closed under inversion,

$$-\mathbf{k} \in \mathcal{K}, \quad \forall \mathbf{k} \in \mathcal{K}, \quad (36)$$

the real-space unitary rotation generated via eq. (13) can be chosen to be real-valued by imposing time-reversal symmetry (TRS) on the k -space generators,

$$\kappa_{\mathbf{k}} = \kappa_{-\mathbf{k}}^*. \quad (37)$$

Throughout this section, $-\mathbf{k}$ is understood as $-\mathbf{k} \bmod \mathbf{G}$ for an appropriate reciprocal lattice vector \mathbf{G} that maps $-\mathbf{k}$ back into the first Brillouin zone.

The TRS constraint in eq. (37) reduces the total number of independent parameters as follows. First, for the $N'_k \leq N_k$ time-reversal invariant points in \mathcal{K} (i.e., those satisfying $\mathbf{k} = -\mathbf{k}$), $\kappa_{\mathbf{k}}$ must be real and skew-symmetric and can therefore be parameterized by $n_{\text{orb}}(n_{\text{orb}} - 1)/2$ real parameters. Second, the remaining k -points can be partitioned into $(N_k - N'_k)/2$ time-reversal pairs $(\mathbf{k}, -\mathbf{k})$ with $\mathbf{k} \neq -\mathbf{k}$; for each pair, only one generator needs to be parameterized explicitly, with its partner fixed by eq. (37). The total number of real parameters in the TRS case thus reduces to

$$\frac{1}{2} N'_k n_{\text{orb}}(n_{\text{orb}} - 1) + \frac{1}{2} (N_k - N'_k) n_{\text{orb}}^2 = \frac{1}{2} (N_k n_{\text{orb}}^2 - N'_k n_{\text{orb}}). \quad (38)$$

The gradient and Hessian–vector product required for k -CIAH optimization under TRS can be obtained directly from

their general forms in eqs. (22) and (23) by symmetrizing with respect to $\mathbf{k} \leftrightarrow -\mathbf{k}$,

$$\bar{G}_{\mathbf{k}ij} = G_{\mathbf{k}ij} + (1 - \delta_{\mathbf{k}, -\mathbf{k}}) G_{-\mathbf{k}ij}^*, \quad (39)$$

$$(\bar{\mathbf{H}}\mathbf{v})_{\mathbf{k}ij} = (\mathbf{H}\mathbf{v})_{\mathbf{k}ij} + (1 - \delta_{\mathbf{k}, -\mathbf{k}}) (\mathbf{H}\mathbf{v})_{-\mathbf{k}ij}^*. \quad (40)$$

The Hessian diagonal elements are modified analogously from eqs. (27) and (28). Specifically, $P_{TA, \mathbf{k}0}$ in eq. (28) is replaced by its TRS-packed form,

$$\bar{P}_{TA, \mathbf{k}0} = P_{TA, \mathbf{k}0} + (1 - \delta_{\mathbf{k}, -\mathbf{k}}) P_{TA, -\mathbf{k}0}^*, \quad (41)$$

and $P_{TA, \mathbf{k}\mathbf{k}}$ is replaced by

$$\bar{P}_{TA, \mathbf{k}\mathbf{k}} = P_{TA, \mathbf{k}\mathbf{k}} + (1 - \delta_{\mathbf{k}, -\mathbf{k}}) [P_{TA, -\mathbf{k}(-\mathbf{k})} + P_{TA, -\mathbf{k}\mathbf{k}}^* + P_{TA, \mathbf{k}(-\mathbf{k})}^*]. \quad (42)$$

In practice, for all systems tested we found that replacing eq. (42) with the following diagonal approximation,

$$\bar{P}_{TA, \mathbf{k}\mathbf{k}} \approx P_{TA, \mathbf{k}\mathbf{k}} + (1 - \delta_{\mathbf{k}, -\mathbf{k}}) P_{TA, -\mathbf{k}(-\mathbf{k})}, \quad (43)$$

does not measurably affect the convergence rate of k -CIAH-based PMWF optimization. This is expected because the Hessian diagonals serve only as a preconditioner for solving the augmented Hessian eigenvalue problem in eq. (18). All numerical results reported in section IV therefore employ the diagonal approximation in eq. (43).

H. Escaping from local stationary points

PMWF optimization can occasionally converge to a local minimum or a saddle point. The efficient Hessian–vector product developed in section II E enables a straightforward stability analysis: one can identify directions of negative curvature and escape saddle points by following the corresponding Hessian eigenvectors. In practice, however, our numerical experiments indicate that most instabilities are dominated by pairwise rotations between WFs, which can be treated effectively with a simple Jacobi sweep algorithm^{31,32} which we describe in this section.

Consider a real-space 2×2 rotation that mixes a WF pair $(w_{0i}, w_{\mathbf{R}j})$ and all of its lattice translates by $\mathbf{R}_0 \in \mathcal{L}$,

$$[\tilde{w}_{\mathbf{R}_0, i} \ \tilde{w}_{\mathbf{R}_0 + \mathbf{R}, j}] = [w_{\mathbf{R}_0, i} \ w_{\mathbf{R}_0 + \mathbf{R}, j}] \begin{bmatrix} \cos \theta & \sin \theta \\ -\sin \theta & \cos \theta \end{bmatrix}. \quad (44)$$

In reciprocal space, eq. (44) is equivalent to applying the following k -dependent rotation to the corresponding Bloch orbital pair,

$$[\tilde{\phi}_{\mathbf{k}i} \ \tilde{\phi}_{\mathbf{k}j}] = [\phi_{\mathbf{k}i} \ \phi_{\mathbf{k}j}] \begin{bmatrix} \cos \theta & e^{i\mathbf{k}\cdot\mathbf{R}} \sin \theta \\ -e^{-i\mathbf{k}\cdot\mathbf{R}} \sin \theta & \cos \theta \end{bmatrix}. \quad (45)$$

A Jacobi-sweep stability check can be constructed by examining all $N_k n_{\text{orb}}^2$ WF pairs $(w_{0i}, w_{\mathbf{R}j})$. This procedure scales as $O(N_k^2 n^3)$, comparable to a single gradient evaluation. In practice, the cost can be further reduced to $O(N_k n^3)$ by restricting

\mathbf{R} in eqs. (44) and (45) to lie within a finite cutoff radius R_{\max} . This truncation is well motivated because pairwise instabilities typically arise between WFs that are spatially close. The working equations for determining the optimal rotation angle θ and details of an efficient implementation are provided in the Supporting Information.

I. Wannier interpolation

An important application of localized WFs is the efficient calculation of electronic band structures via Wannier interpolation.^{4,29} The electronic energy bands $\{\epsilon_{\mathbf{k}i}\}$ are the eigenvalues of the Fock matrix $\{F_{\mathbf{k}ij}\}$ evaluated along a selected k -point path $\mathcal{K}_{\text{Band}}$, typically connecting high-symmetry points in the first Brillouin zone. In a conventional workflow, one first performs a self-consistent-field (SCF) calculation to obtain orbitals on a uniform k -point mesh \mathcal{K}_{SCF} , and then carries out a sequence of non-SCF calculations to construct and diagonalize the Fock matrix at k -points in $\mathcal{K}_{\text{Band}}$. For high-resolution band structures, this approach becomes computationally demanding because it requires a large number of Fock builds.

Wannier interpolation circumvents this bottleneck by enabling efficient band-structure calculations within a chosen energy window. First, the SCF orbitals corresponding to the bands of interest are localized to yield WFs $\{w_{\mathbf{R}i}\}$, with $\{\phi_{\mathbf{k}i}\}$ denoting the associated Bloch orbitals. The real-space Fock matrix in the localized WF basis is then obtained by Fourier transformation,

$$F_{\mathbf{R}i,0j} = \langle w_{\mathbf{R}i} | \hat{F} | w_{0j} \rangle = \sum_{\mathbf{k} \in \mathcal{K}_{\text{SCF}}} \theta_{\mathbf{R}k} F_{\mathbf{k}ij}, \quad (46)$$

where $F_{\mathbf{k}ij} = \langle \phi_{\mathbf{k}i} | \hat{F} | \phi_{\mathbf{k}j} \rangle$ can be obtained via basis transformation from the Fock matrix in the SCF orbital basis. Because localized WFs decay rapidly in real space,^{2,52} one can approximate the Fock matrix at an arbitrary k -point \mathbf{q} by truncating the real-space sum,

$$F_{\mathbf{q}ij} \approx \tilde{F}_{\mathbf{q}ij} = \sum_{\mathbf{R} \in \text{WS}(\mathcal{K}_{\text{SCF}})} \frac{1}{d_{\mathbf{R}}} \theta_{\mathbf{R}q}^* F_{\mathbf{R}ij}. \quad (47)$$

Here, \mathbf{R} runs over the Wigner–Seitz cell associated with the BvK supercell of \mathcal{K}_{SCF} , and the factor $1/d_{\mathbf{R}}$ accounts for degeneracies at the Wigner–Seitz boundary.^{4,29,53} By construction, eq. (47) reproduces the exact SCF Fock matrix for $\mathbf{q} \in \mathcal{K}_{\text{SCF}}$. Diagonalizing $\tilde{F}_{\mathbf{q}ij}$ for $\mathbf{q} \in \mathcal{K}_{\text{Band}}$ yields the Wannier-interpolated band energies $\{\tilde{\epsilon}_{\mathbf{q}i}\}$. We present numerical examples of Wannier interpolation based on PMWFs in section IV C.

III. COMPUTATIONAL DETAILS

We implemented the k -CIAH for PMWF optimization in a developer version of PYSCF,^{50,51} which relies on LIBCINT⁵⁶ for evaluating Gaussian integrals. The orbitals to be localized

TABLE I. Information on the systems used in the numerical tests of this work. For the first six insulating or semiconducting systems, n_{orb} denotes the number of occupied orbitals. For the remaining four metallic systems, Fermi smearing^{54,55} with $\sigma = 0.05$ eV is employed to facilitate SCF convergence; in these cases, n_{orb} is chosen to be the maximum number of bands across all k -points with occupation greater than 10^{-6} .

System	k -mesh	n_{atm}	n_{orb}
h-BN	$15 \times 15 \times 1$	2	4
Diamond	$7 \times 7 \times 7$	2	4
MgO	$7 \times 7 \times 7$	2	8
Silicon	$7 \times 7 \times 7$	2	4
SiO ₂	$3 \times 3 \times 3$	9	24
CO/MgO(001)	$3 \times 3 \times 1$	18	69
<i>trans</i> -(C ₂ H ₂) _∞	$101 \times 1 \times 1$	4	6
C-nanotube	$11 \times 1 \times 1$	32	65
Graphene	$15 \times 15 \times 1$	2	5
Aluminum	$5 \times 5 \times 5$	4	8

are Kohn–Sham orbitals generated with the Perdew–Burke–Ernzerhof (PBE) exchange–correlation functional⁵⁷ on uniform k -point meshes that include the Γ -point. Time-reversal symmetry is enforced in both the mean-field calculations and the PMWF optimization as described in section II G, so that the resulting WFs are real-valued. All calculations employ Goedecker–Teter–Hutter (GTH) pseudopotentials optimized for PBE^{58,59} together with the GTH-cc-pVDZ Gaussian basis sets.⁶⁰ Range-separated density fitting^{61,62} is used to construct the Coulomb matrix.

PMWF optimizations are initialized using the atomic initial guess implemented in PYSCF for the Bloch orbitals at the Γ -point, followed by the phase-alignment procedure described in section II F. The exponent p is set to 2 in all calculations. The optimization is deemed converged when the norm of the gradient falls below 10^{-5} a.u. and that the PM objective value changes by less than 10^{-6} a.u. between successive cycles. The atomic projectors are generated with the meta-Löwdin scheme.³³ Our preliminary tests using alternative choices, such as intrinsic atomic orbitals,³⁴ yield comparable convergence behavior and qualitatively similar WFs to those obtained with meta-Löwdin projectors. This weak sensitivity to the choice of atomic projectors is consistent with previous reports.³⁶ In all PMWF calculations, we perform Hessian- and Jacobi-sweep-based stability analyses after convergence. If an instability is detected, the resulting orbitals are used to reinitialize a subsequent PMWF optimization, which is repeated until a stable solution is obtained. All PMWF calculations were performed using 8 AMD EPYC 7763 CPU cores and a total of 32 GB of memory.

In section IV, we compare the performance of k -CIAH with gradient-based k -BFGS and with molecular CIAH applied directly to the BvK supercell without exploiting translational symmetry between unit cells (hereafter referred to as Γ -CIAH). Our k -BFGS implementation shares the same overall framework as k -CIAH, but employs a modified update step

[cf. eq. (17)],

$$U_k^{(n+1)} = U_k^{(n)} e^{\alpha \kappa_k^{(n+1)}}. \quad (48)$$

Here, the search direction $\kappa_k^{(n+1)}$ is determined by the BFGS scheme,^{39–42} and the step length α is chosen by a line search. For Γ -CIAH, the original PYSCF implementation⁴³ exhibits a formal scaling of $O(N_k^4 n^4)$ because it does not exploit the factorized structure of the atomic projection operator. Following the strategy outlined in section II E for k -CIAH, we implemented an improved Γ -CIAH variant with reduced scaling, $O(N_k^3 n^3)$, which we use for comparison with k -CIAH. Table I summarizes the 10 solid-state systems selected for numerical tests, spanning insulators, semiconductors, (semi)metals, and surfaces. The crystal structures can be found in the Supporting Information.

IV. RESULTS AND DISCUSSION

A. Convergence of k -CIAH-based PMWF optimization

Table II compares the convergence behavior of k -CIAH and k -BFGS for the ten systems listed in table I. Both algorithms converge to the same set of PMWFs, as evidenced by the agreement in the final PM objective values. In all cases, k -CIAH reaches a stable solution directly, whereas k -BFGS initially converges to an unstable solution for MgO, which is subsequently resolved by the stability analysis in section II H.

The number of unitary updates (N_{iter}) required for convergence differs markedly between the two methods: the second-order k -CIAH algorithm typically converges in 5–20 iterations regardless of system type, while the first-order k -BFGS requires 30–300 iterations, roughly an order of magnitude more. The trend observed for k -BFGS here is consistent with previous studies employing BFGS for PMWF optimization.^{35,38} In fig. 1, we illustrate for three challenging systems—SiO₂, CO/MgO(001), and aluminum—that the rapid convergence of k -CIAH stems from its ability to take large steps that drive a fast decay of the gradient norm. By contrast, the gradient norm in k -BFGS fluctuates and rarely exhibits clear superlinear convergence, as also shown in fig. 1.

Table II further compares k -CIAH and k -BFGS in terms of the numbers of gradient (N_g) and Hessian–vector product ($N_{\mathbf{Hv}}$) evaluations. As discussed in section II E, both operations scale as $O(N_k^2 n^3)$ and dominate the overall computational cost. In all cases except MgO, k -CIAH reduces the total $N_g + N_{\mathbf{Hv}}$ relative to k -BFGS, typically by nearly a factor of two. For MgO, k -CIAH requires more $N_g + N_{\mathbf{Hv}}$ evaluations because it effectively performs an internal stability analysis to escape the unstable solution to which k -BFGS initially converges (the cost of this additional stability analysis is not reflected in the N_g reported for k -BFGS in table II). As shown in section IV B, this reduction in $N_g + N_{\mathbf{Hv}}$ translates into a more favorable CPU time to solution for k -CIAH in practice.

Table II also includes results for Γ -CIAH for comparison. For all gapped systems and for two metallic systems (trans-polyacetylene and graphene), Γ -CIAH, heavily assisted by

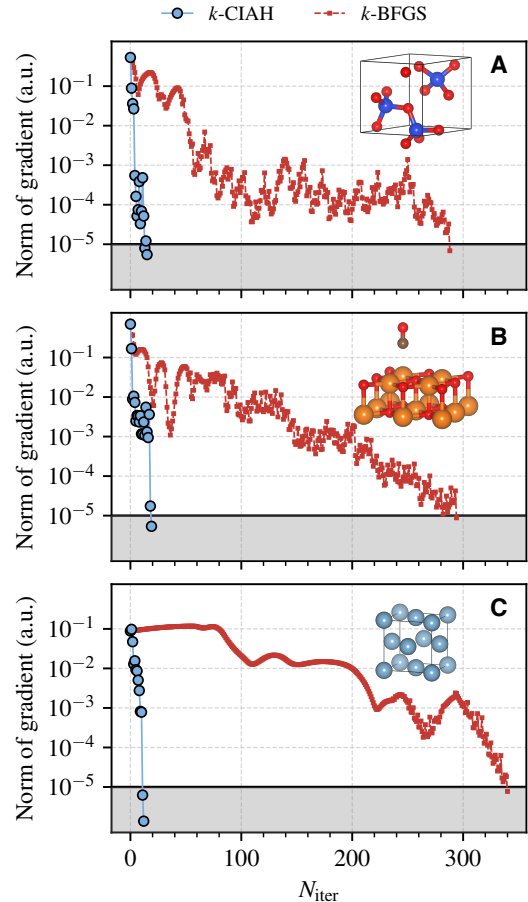


FIG. 1. Convergence of k -CIAH and k -BFGS measured by the decay of the norm of gradient for (A) SiO₂, (B) CO/MgO(001), and (C) aluminum. The convergence threshold (10^{-5}) is denoted by the black horizontal line.

stability analysis, converges to the same translationally invariant PMWFs as k -CIAH, yielding identical PM objective values. For carbon nanotube, however, Γ -CIAH breaks translational symmetry and produces PMWFs with a higher PM objective value. For bulk aluminum, Γ -CIAH fails to converge within 1000 cycles, likely due to a large number of near-degenerate orbitals that render the Hessian ill-conditioned. In cases where both k -CIAH and Γ -CIAH converge, the values of N_{iter} and $N_g + N_{\mathbf{Hv}}$ are comparable between the two approaches. Consequently, because the gradient and Hessian–vector product evaluations in k -CIAH scale as $O(N_k^2 n^3)$ rather than $O(N_k^3 n^3)$, the overall cost of k -CIAH is lower by a factor of $O(N_k)$ relative to Γ -CIAH. This reduction is demonstrated numerically in section IV B.

B. Cost of k -CIAH-based PMWF optimization

Figure 2 compares the CPU time of PMWF optimization using k -CIAH, k -BFGS, and Γ -CIAH for two representative systems: h-BN, which has a small unit cell with four occupied bands to be localized, and CO/MgO(001), which has a

TABLE II. Convergence of PMWF optimization using k -CIAH, k -BFGS, and Γ -CIAH for selected systems. For each method, “PM obj.” denotes the converged PM objective value, N_{iter} is the number of unitary updates defined in eq. (17), and N_g and N_{Hv} are the numbers of gradient and Hessian–vector product evaluations, respectively. For k -BFGS and Γ -CIAH, instabilities are identified in the initially converged orbitals for several systems and are subsequently resolved using the stability analysis developed in section II H. In these cases, N_{iter} lists the iteration counts of all successive PMWF optimizations separated by “+”, whereas N_g and N_{Hv} report the total number of evaluations accumulated over all optimizations. Γ -CIAH failed to converge within 1000 cycles for aluminum.

System	k -CIAH			k -BFGS			Γ -CIAH		
	PM obj.	N_{iter}	$N_g + N_{\text{Hv}}$	PM obj.	N_{iter}	N_g	PM obj.	N_{iter}	$N_g + N_{\text{Hv}}$
h-BN	2.276	3	$11 + 42$	2.276	38	76	2.276	$4 + 3$	$14 + 38$
Diamond	1.859	4	$15 + 62$	1.859	70	140	1.859	$10 + 7$	$37 + 141$
MgO	3.241	9	$24 + 105$	3.241	$27 + 5$	64	3.241	$4 + 3 + 6$	$36 + 152$
Silicon	1.798	5	$18 + 66$	1.798	65	130	1.798	7	$17 + 60$
SiO_2	17.657	15	$40 + 184$	17.657	288	576	17.657	7	$20 + 73$
CO/MgO(001)	61.650	19	$68 + 325$	61.650	294	588	61.650	$7 + 10$	$61 + 267$
<i>trans</i> -(C_2H_2) $_{\infty}$	3.343	4	$13 + 45$	3.343	39	78	3.343	5	$11 + 29$
C-nanotube	28.141	7	$26 + 117$	28.141	93	186	28.163	7	$21 + 88$
Graphene	2.801	5	$22 + 96$	2.801	139	278	2.800	22	$72 + 341$
Aluminum	2.683	12	$52 + 249$	2.684	340	680			Failed

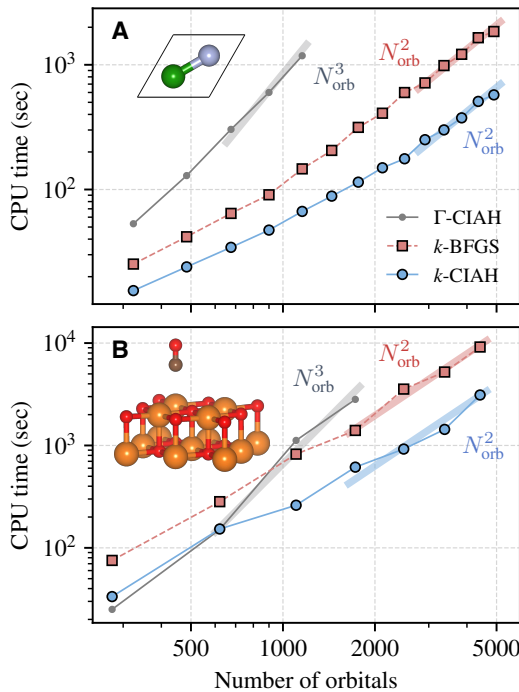


FIG. 2. CPU time (seconds) for PMWF optimization using k -CIAH, k -BFGS, and Γ -CIAH for (A) h-BN and (B) CO/MgO(001). The Brillouin zone is sampled with uniform $n \times n \times 1$ k -meshes, with $n = 9\text{--}35$ for h-BN and $n = 2\text{--}8$ for CO/MgO(001). Fewer data points are shown for Γ -CIAH at large n due to memory limitations. The k -CIAH and k -BFGS timings are fitted to an $O(N_{\text{orb}}^2)$ scaling, whereas the Γ -CIAH data are fitted to an $O(N_{\text{orb}}^3)$ scaling.

larger unit cell with 69 occupied bands. In both cases, we increase the system size by uniformly refining the k -mesh in the xy plane. Linear fits in log–log scale confirm the ex-

pected asymptotic behavior: k -CIAH and k -BFGS exhibit quadratic scaling with N_{orb} , whereas Γ -CIAH shows cubic scaling. Consistent with the reduction in $N_g + N_{\text{Hv}}$ discussed in section IV B, k -CIAH is faster than k -BFGS by approximately a factor of two to three for both systems. For h-BN, both k -point methods are substantially faster than Γ -CIAH due to the small number of occupied bands. As the band count increases, however, the performance gap between the k -point and Γ -point approaches narrows: for CO/MgO(001), Γ -CIAH remains more efficient than k -BFGS up to roughly 1000 localized orbitals. Nevertheless, k -CIAH retains a clear advantage over Γ -CIAH across the range of system sizes considered here.

C. Wannier interpolation for band structure calculations

We demonstrate the use of PMWFs for electronic band structure calculations via the Wannier interpolation procedure outlined in section III. Figure 3(A–D) compares PMWF-interpolated bands with reference bands obtained from non-SCF calculations for h-BN using different SCF k -meshes. As the SCF k -mesh is refined, the PMWF-interpolated bands rapidly approach the reference bands, yielding high-quality band structures even for a relatively coarse 5×5 mesh (fig. 3B). By contrast, interpolation based on WFs constructed directly from Kohn–Sham orbitals without PM localization (hereafter KSWFs) exhibits noticeable deviations from the reference bands especially at band crossing points, even for a 9×9 SCF k -mesh.

Figure 3(E) quantifies the band-interpolation error by reporting the mean absolute error of the highest-occupied band (HOB) and lowest-unoccupied band (LUB) as a function of the SCF k -mesh size for both PMWF- and KSWF-based in-

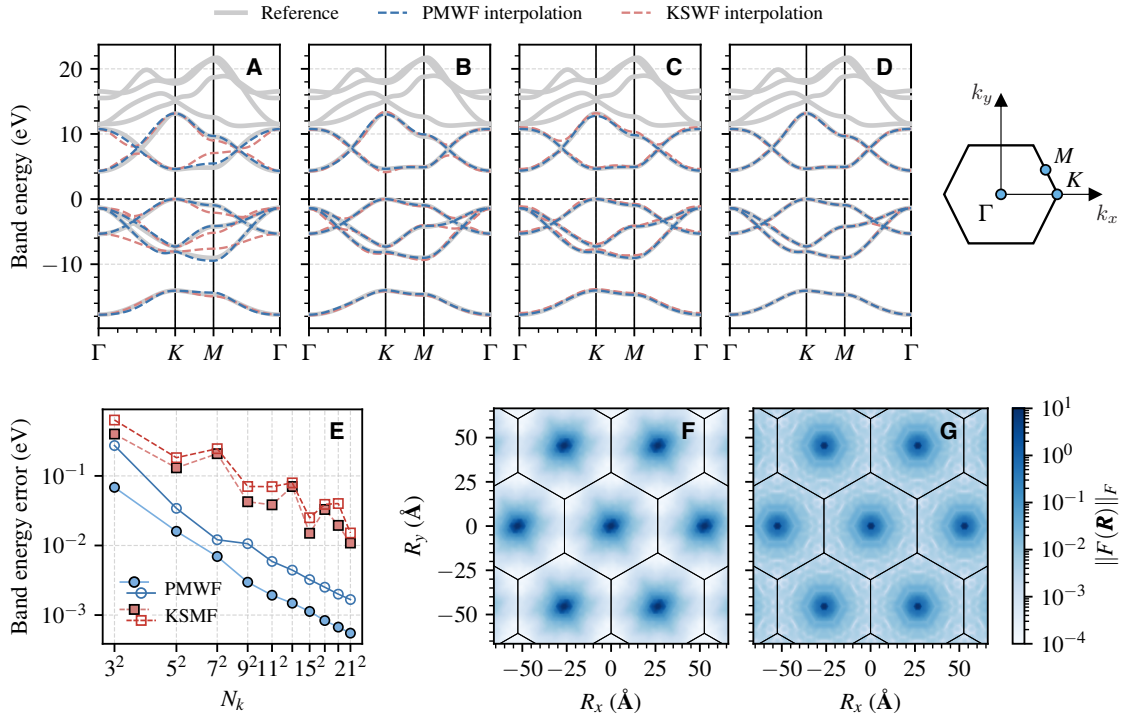


FIG. 3. (A–D) Electronic band structure of h-BN obtained from reference non-SCF calculations (gray) and from Wannier interpolation using PMWFs generated by k -CIAH (blue) for increasing SCF k -mesh sizes: (A) 3×3 , (B) 5×5 , (C) 7×7 , and (D) 9×9 . For comparison, bands interpolated using Kohn–Sham-based WFs without PM localization (KSWFs) are shown in red. In all cases, four occupied and two virtual bands are included in the interpolation. The high-symmetry points in the first Brillouin zone are indicated on the right. (E) Mean absolute error of the interpolated highest-occupied band (HOB; filled markers) and lowest-unoccupied band (LUB; hollow markers) as a function of SCF k -mesh size for h-BN. (F–G) Frobenius norm of the real-space Fock matrix $\|F(\mathbf{R})\|_F$ in the basis of (F) PMWFs and (G) KSWFs, visualized as two-dimensional heat maps for h-BN using a 21×21 SCF k -mesh. Black lines delineate the boundaries of the Wigner–Seitz cells.

terpolation. For PMWFs, the error drops well below 0.1 eV already at a 5×5 k -mesh and decreases monotonically upon further k -mesh refinement. In contrast, the error decay for KSWF-based interpolation is more erratic and significantly slower, typically requiring SCF k -meshes roughly an order of magnitude denser to reach comparable accuracy. This comparison underscores the importance of orbital localization for reliable Wannier interpolation.

The different interpolation accuracy of PMWFs and KSWFs can be rationalized by examining the spatial decay of the real-space Fock matrix elements defined in eq. (46). Figure 3(F,G) shows $\|F(\mathbf{R})\|_F$ (i.e., the Frobenius norm) in both the PMWF and KSWF bases for h-BN with a 21×21 SCF k -mesh. In both representations, the Fock matrix elements decay as one moves from the center toward the boundary of a Wigner–Seitz cell. However, the decay is substantially faster in the PMWF basis than in the KSWF basis, which explains the superior band-interpolation performance of PMWFs.

V. CONCLUSION

In summary, we have developed a k -point extension of the second-order co-iterative augmented Hessian algorithm, termed k -CIAH, for Pipek–Mezey localization of Wannier

functions. Through an efficient evaluation of the Hessian–vector product, k -CIAH achieves $O(N_k^2 n^3)$ scaling in both CPU time and memory, matching that of first-order approaches reported previously^{35,38} while improving upon the $O(N_k^3 n^3)$ scaling of Γ -point CIAH.⁴³ Benchmark calculations on a diverse set of solids demonstrate the fast and robust convergence of k -CIAH, making its overall computational efficiency competitive with that of k -BFGS and Γ -CIAH. The quality of the resulting PMWFs is further validated by accurate electronic band structures obtained via PMWF-based Wannier interpolation.

Several avenues for future work remain. First, the current $O(N_k^2)$ dependence on the k -mesh size can, in principle, be reduced to $O(N_k)$ by adopting a real-space formulation that explicitly exploits the locality of WFs.⁶³ This reduction would benefit both k -CIAH and k -BFGS and enable applications to substantially larger systems than those considered here. Second, orbital localization underpins many reduced-scaling correlated wavefunction methods,^{19–25,64,65} whose application to periodic solids has expanded rapidly over the past decade. High-quality localized WFs may therefore have a significant impact on local correlation treatments of challenging systems, such as metals, bulk defects, and solid interfaces. Finally, the k -CIAH framework developed in this work can be extended to other periodic calculations that involve orbital optimization,

most notably second-order SCF methods.⁶⁶

SUPPORTING INFORMATION

See the Supporting Information for (i) structural files, (ii) derivation of analytical gradient, Hessian–vector product, and Hessian diagonals of the PM objective function, and (iii) derivation of a Jacobi-sweep-based stability analysis.

CONFLICT OF INTEREST

The authors declare no competing conflicts of interest.

DATA AVAILABILITY

The data that support the findings of this study are available from the corresponding author upon reasonable request.

ACKNOWLEDGMENTS

This work was supported by the startup funds from the University of Maryland, College Park. We are grateful for Timothy C. Berkelbach and Qiming Sun for helpful discussion. We acknowledge computing resources provided by the Division of Information Technology at the University of Maryland, College Park.

- ¹G. H. Wannier, “The structure of electronic excitation levels in insulating crystals,” *Phys. Rev.* **52**, 191–197 (1937).
- ²W. Kohn, “Analytic properties of bloch waves and wannier functions,” *Phys. Rev.* **115**, 809–821 (1959).
- ³X. Wang, J. R. Yates, I. Souza, and D. Vanderbilt, “Ab initio calculation of the anomalous hall conductivity by wannier interpolation,” *Phys. Rev. B* **74**, 195118 (2006).
- ⁴J. R. Yates, X. Wang, D. Vanderbilt, and I. Souza, “Spectral and fermi surface properties from wannier interpolation,” *Phys. Rev. B* **75**, 195121 (2007).
- ⁵F. Giustino, M. L. Cohen, and S. G. Louie, “Electron-phonon interaction using wannier functions,” *Phys. Rev. B* **76**, 165108 (2007).
- ⁶I. V. Solovyev, Z. V. Pchelkina, and V. I. Anisimov, “Construction of wannier functions from localized atomiclike orbitals,” *Phys. Rev. B* **75**, 045110 (2007).
- ⁷C. Franchini, R. Kováčik, M. Marsman, S. Sathyaranayana Murthy, J. He, C. Ederer, and G. Kresse, “Maximally localized wannier functions in lamno3 within pbe + u, hybrid functionals and partially self-consistent gw: an efficient route to construct ab initio tight-binding parameters for eg perovskites,” *J. Phys.: Condens. Matter* **24**, 235602 (2012).
- ⁸S. Jiang, D. J. Scalapino, and S. R. White, “Density matrix renormalization group based downfolding of the three-band hubbard model: Importance of density-assisted hopping,” *Phys. Rev. B* **108**, L161111 (2023).
- ⁹I. Mosquera-Lois, S. R. Kavanagh, A. M. Ganose, and A. Walsh, “Machine-learning structural reconstructions for accelerated point defect calculations,” *npjCM* **10**, 121 (2024).
- ¹⁰A. M. Alvertis, A. Khan, and N. M. Tubman, “Compressing hamiltonians with ab initio downfolding for simulating strongly-correlated materials on quantum computers,” *Phys. Rev. Appl.* **23**, 044028 (2025).
- ¹¹L. Zhang, H. Wang, M. C. Muniz, A. Z. Panagiotopoulos, R. Car, and W. E, “A deep potential model with long-range electrostatic interactions,” *J. Chem. Phys.* **156**, 124107 (2022).

¹²A. Gao and R. C. Remsing, “Self-consistent determination of long-range electrostatics in neural network potentials,” *Nat. Commun.* **13**, 1572 (2022).

¹³R. Gao, Y. Li, and R. Car, “Enhanced deep potential model for fast and accurate molecular dynamics: application to the hydrated electron,” *Phys. Chem. Chem. Phys.* **26**, 23080–23088 (2024).

¹⁴B. Amadon, F. Lechermann, A. Georges, F. Jollet, T. O. Wehling, and A. I. Lichtenstein, “Plane-wave based electronic structure calculations for correlated materials using dynamical mean-field theory and projected local orbitals,” *Phys. Rev. B* **77**, 205112 (2008).

¹⁵Z.-H. Cui, T. Zhu, and G. K.-L. Chan, “Efficient implementation of ab initio quantum embedding in periodic systems: Density matrix embedding theory,” *J. Chem. Theory Comput.* **16**, 119–129 (2020).

¹⁶T. Zhu, Z.-H. Cui, and G. K.-L. Chan, “Efficient formulation of ab initio quantum embedding in periodic systems: Dynamical mean-field theory,” *J. Chem. Theory Comput.* **16**, 141–153 (2020).

¹⁷T. Schäfer, F. Libisch, G. Kresse, and A. Grüneis, “Local embedding of coupled cluster theory into the random phase approximation using plane waves,” *J. Chem. Phys.* **154**, 011101 (2021).

¹⁸T. Schäfer, A. Gallo, A. Irmel, F. Hummel, and A. Grüneis, “Surface science using coupled cluster theory via local wannier functions and in-rpa-embedding: The case of water on graphitic carbon nitride,” *J. Chem. Phys.* **155**, 244103 (2021).

¹⁹A. Nejad, A. Zhu, K. Sorathia, and D. P. Tew, “Dlpno-mp2 for periodic systems. i. periodic boundary conditions,” *J. Chem. Phys.* **163**, 214107 (2025).

²⁰A. Zhu, A. Nejad, P. Komonvasee, K. Sorathia, and D. P. Tew, “Dlpno-mp2 for periodic systems. ii. megacell embedding,” *J. Chem. Phys.* **163**, 214108 (2025).

²¹A. Zhu, P. Komonvasee, A. Nejad, and D. P. Tew, “Surface adsorption at the thermodynamic limit using periodic dlpno-mp2 theory: A study of co on mgo at dilute and dense coverages,” arXiv preprint arXiv:2512.23879 (2025), [arXiv:2512.23879 \[physics.chem-ph\]](https://arxiv.org/abs/2512.23879).

²²H.-Z. Ye and T. C. Berkelbach, “*Ab Initio* surface chemistry with chemical accuracy: Application to water on metal oxides,” arXiv preprint arXiv:2309.14640 (2023).

²³H.-Z. Ye and T. C. Berkelbach, “Adsorption and vibrational spectroscopy of co on the surface of mgo from periodic local coupled-cluster theory,” *Faraday Discuss.* **254**, 628–640 (2024).

²⁴H.-Z. Ye and T. C. Berkelbach, “Periodic local coupled-cluster theory for insulators and metals,” *Journal of Chemical Theory and Computation* **20**, 8948–8959 (2024).

²⁵A. S. Hansen, E. Aubakken, and T. B. Pedersen, “Smooth potential-energy surfaces in fragmentation-based local correlation methods for periodic systems,” *Mol. Phys.* **119**, e1896046 (2021).

²⁶J. M. Foster and S. F. Boys, “Canonical configurational interaction procedure,” *Rev. Mod. Phys.* **32**, 300–302 (1960).

²⁷N. Marzari and D. Vanderbilt, “Maximally localized generalized wannier functions for composite energy bands,” *Phys. Rev. B* **56**, 12847–12865 (1997).

²⁸I. Souza, N. Marzari, and D. Vanderbilt, “Maximally localized wannier functions for entangled energy bands,” *Phys. Rev. B* **65**, 035109 (2001).

²⁹N. Marzari, A. A. Mostofi, J. R. Yates, I. Souza, and D. Vanderbilt, “Maximally localized wannier functions: Theory and applications,” *Rev. Mod. Phys.* **84**, 1419–1475 (2012).

³⁰I.-M. Høyvik, B. Jansik, and P. Jørgensen, “Orbital localization using fourth central moment minimization,” *J. Chem. Phys.* **137**, 224114 (2012).

³¹C. Edmiston and K. Ruedenberg, “Localized atomic and molecular orbitals,” *Rev. Mod. Phys.* **35**, 457–464 (1963).

³²J. Pipek and P. G. Mezey, “A fast intrinsic localization procedure applicable for ab initio and semiempirical linear combination of atomic orbital wave functions,” *J. Chem. Phys.* **90**, 4916–4926 (1989).

³³Q. Sun and G. K.-L. Chan, “Exact and optimal quantum mechanics/molecular mechanics boundaries,” *J. Chem. Theory Comput.* **10**, 3784–3790 (2014).

³⁴G. Knizia, “Intrinsic atomic orbitals: An unbiased bridge between quantum theory and chemical concepts,” *J. Chem. Theory Comput.* **9**, 4834–4843 (2013).

³⁵M. C. Clement, X. Wang, and E. F. Valeev, “Robust pipek–mezey orbital localization in periodic solids,” *J. Chem. Theory Comput.* **17**, 7406–7415 (2021).

³⁶S. Lehtola and H. Jónsson, “Pipek–mezey orbital localization using various partial charge estimates,” *J. Chem. Theory Comput.* **10**, 642–649 (2014).

³⁷E. Ö. Jónsson, S. Lehtola, M. Puska, and H. Jónsson, “Theory and applications of generalized pipek–mezey wannier functions,” *J. Chem. Theory Comput.* **13**, 460–474 (2017).

³⁸A. Zhu and D. P. Tew, “Wannier function localization using bloch intrinsic atomic orbitals,” *J. Phys. Chem. A* **128**, 8570–8579 (2024).

³⁹C. G. Broyden, “The convergence of a class of double-rank minimization algorithms. i. general considerations,” *IMA J. Appl. Math.* **6**, 76–90 (1970).

⁴⁰R. Fletcher, “A new approach to variable metric algorithms,” *Comput. J.* **13**, 317–322 (1970).

⁴¹D. Goldfarb, “A family of variable-metric methods derived by variational means,” *Math. Comput.* **24**, 23–26 (1970).

⁴²D. F. Shanno, “Conditioning of quasi-newton methods for function minimization,” *Math. Comput.* **24**, 647–656 (1970).

⁴³Q. Sun, “Co-iterative augmented hessian method for orbital optimization,” arXiv preprint arXiv:1610.08423 (2016), [arXiv:1610.08423 \[physics.chem-ph\]](https://arxiv.org/abs/1610.08423).

⁴⁴Q. Sun, J. Yang, and G. K.-L. Chan, “A general second order complete active space self-consistent-field solver for large-scale systems,” *Chem. Phys. Lett.* **683**, 291–299 (2017), ahmed Zewail (1946–2016) Commemoration Issue of Chemical Physics Letters.

⁴⁵R. Song, X. Gong, A. Bakry, and H.-Z. Ye, “Random phase approximation-based local natural orbital coupled cluster theory,” arXiv preprint arXiv:2601.00131 (2025), [arXiv:2601.00131 \[physics.chem-ph\]](https://arxiv.org/abs/2601.00131).

⁴⁶I.-M. Höyvik, B. Jansik, and P. Jørgensen, “Trust region minimization of orbital localization functions,” *J. Chem. Theory Comput.* **8**, 3137–3146 (2012).

⁴⁷E. R. Davidson, “The iterative calculation of a few of the lowest eigenvalues and corresponding eigenvectors of large real-symmetric matrices,” *J. Comput. Phys.* **17**, 87–94 (1975).

⁴⁸F. Aquilante, T. Bondo Pedersen, A. Sánchez de Merás, and H. Koch, “Fast noniterative orbital localization for large molecules,” *J. Chem. Phys.* **125**, 174101 (2006).

⁴⁹P. Pulay, “Localizability of dynamic electron correlation,” *Chem. Phys. Lett.* **100**, 151–154 (1983).

⁵⁰Q. Sun, T. C. Berkelbach, N. S. Blunt, G. H. Booth, S. Guo, Z. Li, J. Liu, J. D. McClain, E. R. Sayfutyarova, S. Sharma, S. Wouters, and G. K.-L. Chan, “Pyscf: the python-based simulations of chemistry framework,” *Wiley Interdiscip. Rev. Comput. Mol. Sci.* **8**, e1340 (2018).

⁵¹Q. Sun, X. Zhang, S. Banerjee, P. Bao, M. Barbry, N. S. Blunt, N. A. Bogdanov, G. H. Booth, J. Chen, Z.-H. Cui, J. J. Eriksen, Y. Gao, S. Guo, J. Hermann, M. R. Hermes, K. Koh, P. Koval, S. Lehtola, Z. Li, J. Liu, N. Mardirossian, J. D. McClain, M. Motta, B. Mussard, H. Q. Pham, A. Pulkin, W. Purwanto, P. J. Robinson, E. Ronca, E. R. Sayfutyarova, M. Scheurer, H. F. Schurkus, J. E. T. Smith, C. Sun, S.-N. Sun, S. Upadhyay, L. K. Wagner, X. Wang, A. White, J. D. Whitfield, M. J. Williamson, S. Wouters, J. Yang, J. M. Yu, T. Zhu, T. C. Berkelbach, S. Sharma, A. Y. Sokolov, and G. K.-L. Chan, “Recent developments in the PySCF program package,” *J. Chem. Phys.* **153**, 024109 (2020).

⁵²L. He and D. Vanderbilt, “Exponential decay properties of wannier functions and related quantities,” *Phys. Rev. Lett.* **86**, 5341–5344 (2001).

⁵³A. A. Mostofi, J. R. Yates, Y.-S. Lee, I. Souza, D. Vanderbilt, and N. Marzari, “wannier90: A tool for obtaining maximally-localised wannier functions,” *Comput. Phys. Commun.* **178**, 685–699 (2008).

⁵⁴M. J. Gillan, “Calculation of the vacancy formation energy in aluminium,” *J. Phys.: Condens. Matter* **1**, 689 (1989).

⁵⁵F. J. dos Santos and N. Marzari, “Fermi energy determination for advanced smearing techniques,” *Phys. Rev. B* **107**, 195122 (2023).

⁵⁶Q. Sun, “Libcint: An efficient general integral library for gaussian basis functions,” *J. Comput. Chem.* **36**, 1664–1671 (2015).

⁵⁷J. P. Perdew, K. Burke, and M. Ernzerhof, “Generalized gradient approximation made simple,” *Phys. Rev. Lett.* **77**, 3865–3868 (1996).

⁵⁸S. Goedecker, M. Teter, and J. Hutter, “Separable dual-space gaussian pseudopotentials,” *Phys. Rev. B* **54**, 1703–1710 (1996).

⁵⁹C. Hartwigsen, S. Goedecker, and J. Hutter, “Relativistic separable dual-space gaussian pseudopotentials from h to rn,” *Phys. Rev. B* **58**, 3641–3662 (1998).

⁶⁰H.-Z. Ye and T. C. Berkelbach, “Correlation-consistent gaussian basis sets for solids made simple,” *J. Chem. Theory Comput.* **18**, 1595–1606 (2022).

⁶¹H.-Z. Ye and T. C. Berkelbach, “Fast periodic Gaussian density fitting by range separation,” *J. Chem. Phys.* **154**, 131104 (2021).

⁶²H.-Z. Ye and T. C. Berkelbach, “Tight distance-dependent estimators for screening two-center and three-center short-range Coulomb integrals over Gaussian basis functions,” *J. Chem. Phys.* **155**, 124106 (2021).

⁶³G. Weng, M. Romanova, A. Apelian, H. Song, and V. Vlček, “Reduced scaling of optimal regional orbital localization via sequential exhaustion of the single-particle space,” *J. Chem. Theory Comput.* **18**, 4960–4972 (2022).

⁶⁴B. T. G. Lau, G. Knizia, and T. C. Berkelbach, “Regional embedding enables high-level quantum chemistry for surface science,” *J. Phys. Chem. Lett.* **12**, 1104–1109 (2021).

⁶⁵Z. Huang, Z. Guo, C. Cao, H. Q. Pham, X. Wen, G. H. Booth, J. Chen, and D. Lv, “A multi-resolution systematically improvable quantum embedding scheme for large-scale surface chemistry calculations,” *Nat. Commun.* **16**, 9297 (2025).

⁶⁶H. Werner and P. J. Knowles, “A second order multiconfiguration scf procedure with optimum convergence,” *J. Chem. Phys.* **82**, 5053–5063 (1985).

Supporting Information for Fast Generation of Pipek–Mezey Wannier Functions via the Co-Iterative Augmented Hessian Method

Gengzhi Yang^{1,2} and Hong-Zhou Ye^{3,4, a)}

¹⁾*Joint Center for Quantum Information and Computer Science, University of Maryland, College Park, Maryland, 20742*

²⁾*Department of Mathematics, University of Maryland, College Park, Maryland, 20742*

³⁾*Department of Chemistry and Biochemistry, University of Maryland, College Park, Maryland, 20742*

⁴⁾*Institute for Physical Science and Technology, University of Maryland, College Park, Maryland, 20742*

(Dated: 16 February 2026)

^{a)}Electronic mail: hzye@umd.edu

CONTENTS

I. Structure files	3
II. Derivation of analytical gradients, Hessian–vector product, and Hessian diagonals	3
A. Parameterization	3
B. Basic derivatives	3
C. Cost function	4
D. Gradient	4
E. Hessian–vector product	5
1. Disconnected term	5
2. Connected symmetric term	6
3. Connected asymmetric term	6
F. Hessian diagonal	7
1. Disconnected term	7
2. Connected asymmetric term	8
3. Connected symmetric term	8
III. Jacobi sweep	9
A. General consideration	9
B. Working equations for $p = 2$	9
C. Extension for $p > 2$	10
D. Efficient implementation and computational cost	11

I. STRUCTURE FILES

The structure files for all solid-state systems studied in this work are available in the following GitHub repository:

https://github.com/hongzhouye/supporting_data/tree/main/2026/PMWF

where

- the structure of h-BN, diamond, MgO, silicon, SiO₂, *trans*-(C₂H₂)_∞, C-nanotube, and graphene is taken from *J. Phys. Chem. A* **128**, 8570 (2024),
- the structure of CO/MgO(001) is taken from *Faraday Discuss.* **254**, 628 (2024),
- and the structure of aluminum (*fcc*) is generated with a lattice constant of 4.05 Å.

II. DERIVATION OF ANALYTICAL GRADIENTS, HESSIAN-VECTOR PRODUCT, AND HESSIAN DIAGONALS

A. Parameterization

As discussed in the main text, the k -space unitaries can be parameterized using k -dependent generators, each of which is a complex anti-Hermitian matrix. Let $\kappa_{\mathbf{k}} = X_{\mathbf{k}} + i Y_{\mathbf{k}}$ where both $X_{\mathbf{k}}$ and $Y_{\mathbf{k}} \in \mathbb{R}^{n_{\text{orb}} \times n_{\text{orb}}}$. The unique parameters are the lower-triangular part of $X_{\mathbf{k}}$, excluding the diagonals, and the the lower-triangular part of $Y_{\mathbf{k}}$, including the diagonals.

B. Basic derivatives

Define $(E_{mn})_{ij} = \delta_{mi}\delta_{nj}$. The first- and second-order derivatives of the unitary with respect to the generators evaluated at $\kappa_{\mathbf{k}} = 0$ are

$$\begin{aligned} \frac{\partial U_{\mathbf{k}'}}{\partial X_{\mathbf{k}mn}} &= \delta_{\mathbf{kk}'}(E_{mn} - E_{nm}), & (m \neq n) \\ \frac{\partial U_{\mathbf{k}'}}{\partial Y_{\mathbf{k}mn}} &= i\delta_{\mathbf{kk}'}(E_{mn} + E_{nm}), & (m \neq n) \\ \frac{\partial U_{\mathbf{k}'}}{\partial Y_{\mathbf{k}mm}} &= i\delta_{\mathbf{kk}'}E_{mm}. \end{aligned} \quad (1)$$

$$\frac{\partial^2 U_{\mathbf{k}''}}{\partial A_{\mathbf{k}mn} B_{\mathbf{k}'pq}} = \frac{1}{2} \left\{ \frac{\partial U_{\mathbf{k}''}}{\partial A_{\mathbf{k}mn}}, \frac{\partial U_{\mathbf{k}''}}{\partial B_{\mathbf{k}'mn}} \right\}, \quad (A, B = X, Y) \quad (2)$$

C. Cost function

The PM objective function defined in the main text here is recapped here. A minus sign is added to the objective function to turn the maximization a minimization problem.

$$L = - \sum_{\mathbf{T}_{A,i}} Q_{\mathbf{T}_{A,0i}}^p \quad (3)$$

$$Q_{\mathbf{T}_{A,0i}} = P_{\mathbf{T}_{A,0i},0i} = \sum_{\mathbf{k}\mathbf{k}'} \left(U_{\mathbf{k}}^\dagger P_{\mathbf{T}_{A,\mathbf{k}\mathbf{k}'}} U_{\mathbf{k}'} \right)_{ii} \quad (4)$$

$$P_{\mathbf{T}_{A,\mathbf{k}\mathbf{k}'}} = \frac{1}{N_k} \sum_{\mathbf{R}\mathbf{R}'} \theta_{\mathbf{R}\mathbf{k}}^* P_{\mathbf{T}_{A,\mathbf{R}\mathbf{R}'}} \theta_{\mathbf{R}'\mathbf{k}'} \quad (5)$$

D. Gradient

Consider the first-order variation of L ,

$$\delta L = -p \sum_{\mathbf{T}_{A,i}} Q_{\mathbf{T}_{A,0i}}^{p-1} \delta Q_{\mathbf{T}_{A,0i}} \quad (6)$$

which depends on the first-order variation of Q ,

$$\delta Q_{\mathbf{T}_{A,0i}} = 2\Re \sum_{\mathbf{k}'} \left(P_{\mathbf{T}_{A,0\mathbf{k}'}} \delta U_{\mathbf{k}'} \right)_{ii}, \quad \left(P_{\mathbf{T}_{A,0\mathbf{k}'}} := \sum_{\mathbf{k}} P_{\mathbf{T}_{A,\mathbf{k}\mathbf{k}'}} \right) \quad (7)$$

For the real and imaginary part of the generator, the derivatives are

$$\begin{aligned} \frac{\partial Q_{\mathbf{T}_{A,0i}}}{\partial X_{\mathbf{k}mn}} &= -2 \left(P_{\mathbf{T}_{A,0m},\mathbf{k}n}^{\Re} \delta_{mi} - P_{\mathbf{T}_{A,0n},\mathbf{k}m}^{\Re} \delta_{ni} \right) \\ \frac{\partial Q_{\mathbf{T}_{A,0i}}}{\partial Y_{\mathbf{k}mn}} &= -2 \left(P_{\mathbf{T}_{A,0m},\mathbf{k}n}^{\Im} \delta_{mi} + P_{\mathbf{T}_{A,0n},\mathbf{k}m}^{\Im} \delta_{ni} \right) \end{aligned} \quad (8)$$

The two can be combined conveniently into a complex-valued expression,

$$\frac{\partial Q_{\mathbf{T}_{A,0i}}}{\partial X_{\mathbf{k}mn}} + i \frac{\partial Q_{\mathbf{T}_{A,0i}}}{\partial Y_{\mathbf{k}mn}} = -2 \left(P_{\mathbf{T}_{A,0m},\mathbf{k}n} \delta_{mi} - P_{\mathbf{T}_{A,0n},\mathbf{k}m}^* \delta_{ni} \right) \quad (9)$$

which leads to the following expression for the gradient,

$$G_{\mathbf{k}} = \tilde{G}_{\mathbf{k}} - \tilde{G}_{\mathbf{k}}^\dagger,$$

$$\tilde{G}_{\mathbf{k}mn} = 2p \sum_{\mathbf{T}_A} Q_{\mathbf{T}_{A,0m}}^{p-1} P_{\mathbf{T}_{A,0m},\mathbf{k}n}$$

(10)

Using $P_{\mathbf{T}_{A,\mathbf{k}0}} = P_{\mathbf{T}_{A,0\mathbf{k}}}^\dagger$, one can convert eq. (10) to Eqn M22 in the main text. We prefer to put \mathbf{k} index first as in $P_{\mathbf{T}_{A,\mathbf{k}0}}$ due to the C-ordering of matrices and tensors in our code.

E. Hessian–vector product

Let $v_{\mathbf{k}}$ denote the vector to be applied by the Hessian. Let $v_{\mathbf{k}}^X$ and $v_{\mathbf{k}}^Y$ denote its real and imaginary parts, respectively. The Hessian–vector product is defined as follows.

$$\begin{aligned}\Sigma_{\mathbf{k}mn}^X &= \frac{1}{2} \sum_{\mathbf{k}'pq} \frac{\partial^2 L}{\partial X_{\mathbf{k}mn} \partial X_{\mathbf{k}'pq}} v_{\mathbf{k}'pq}^X + \frac{\partial^2 L}{\partial X_{\mathbf{k}mn} \partial Y_{\mathbf{k}'pq}} v_{\mathbf{k}'pq}^Y, \\ \Sigma_{\mathbf{k}mn}^Y &= \frac{1}{2} \sum_{\mathbf{k}'pq} \frac{\partial^2 L}{\partial Y_{\mathbf{k}mn} \partial X_{\mathbf{k}'pq}} v_{\mathbf{k}'pq}^X + \frac{\partial^2 L}{\partial Y_{\mathbf{k}mn} \partial Y_{\mathbf{k}'pq}} v_{\mathbf{k}'pq}^Y,\end{aligned}\tag{11}$$

where at a high-level, we need to evaluate the second-order variation of L ,

$$\delta^2 L = -p(p-1) \sum_{TAi} Q_{TA,0i}^{p-2} (\delta Q_{TA,0i})^2 - p \sum_{TAi} Q_{TA,0i}^{p-1} \delta^2 Q_{TA,0i}\tag{12}$$

The first term only depends on the first-order variation of Q , whose expression has already been derived above. We call this term *disconnected*. The second term depends on the second-order variation of Q ,

$$\delta^2 Q_{TA,0i} = 2\Re \sum_{\mathbf{k}'} \left(P_{TA,0\mathbf{k}'} \delta^2 U_{\mathbf{k}'} \right)_{ii} + 2\Re \sum_{\mathbf{k}\mathbf{k}'} \left(\delta U_{\mathbf{k}}^\dagger P_{TA,\mathbf{k}\mathbf{k}'} \delta U_{\mathbf{k}'} \right)_{ii}\tag{13}$$

and therefore is *connected*. We further differentiate the first and second term in $\delta^2 Q$ to be *asymmetric* and *symmetric* connected terms.

1. Disconnected term

$$\begin{aligned}\Sigma_{\mathbf{k}mn}^X &= -\frac{1}{2} p(p-1) \sum_{TAi} Q_{TA,0i}^{p-2} \frac{\partial Q_{TA,0i}}{\partial X_{\mathbf{k}mn}} \sum_{\mathbf{k}'pq} \left(\frac{\partial Q_{TA,0i}}{\partial X_{\mathbf{k}'pq}} v_{\mathbf{k}'pq}^X + \frac{\partial Q_{TA,0i}}{\partial Y_{\mathbf{k}'pq}} v_{\mathbf{k}'pq}^Y \right), \\ \Sigma_{\mathbf{k}mn}^Y &= -\frac{1}{2} p(p-1) \sum_{TAi} Q_{TA,0i}^{p-2} \frac{\partial Q_{TA,0i}}{\partial Y_{\mathbf{k}mn}} \sum_{\mathbf{k}'pq} \left(\frac{\partial Q_{TA,0i}}{\partial X_{\mathbf{k}'pq}} v_{\mathbf{k}'pq}^X + \frac{\partial Q_{TA,0i}}{\partial Y_{\mathbf{k}'pq}} v_{\mathbf{k}'pq}^Y \right)\end{aligned}\tag{14}$$

where the term in the parenthesis can be simplified to

$$\sum_{\mathbf{k}'pq} \left(\frac{\partial Q_{TA,0i}}{\partial X_{\mathbf{k}'pq}} v_{\mathbf{k}'pq}^X + \frac{\partial Q_{TA,0i}}{\partial Y_{\mathbf{k}'pq}} v_{\mathbf{k}'pq}^Y \right) = 4\Re \sum_{\mathbf{k}'} \left(P_{TA,0\mathbf{k}'} v_{\mathbf{k}'} \right)_{ii}\tag{15}$$

Combining this with the gradient of Q [eq. (8)] gives

$$\begin{aligned}\Sigma_{\mathbf{k}} &= \tilde{\Sigma}_{\mathbf{k}} - \tilde{\Sigma}_{\mathbf{k}}, \\ \tilde{\Sigma}_{\mathbf{k}mn} &= 4p(p-1) \sum_{TA} Q_{TA,0m}^{p-2} \sum_{\mathbf{k}'} \Re(P_{TA,0\mathbf{k}'} v_{\mathbf{k}'})_{mm} P_{TA,0m,\mathbf{k}n}\end{aligned}\tag{16}$$

2. Connected symmetric term

$$\begin{aligned}\Sigma_{\mathbf{k}mn}^X &= -p \sum_{\mathbf{T}A,i} Q_{\mathbf{T}A,\mathbf{0}i}^{p-1} \Re \left[\frac{\partial U_{\mathbf{k}}^\dagger}{\partial X_{\mathbf{k}mn}} P_{\mathbf{T}A,\mathbf{kk}'} \sum_{\mathbf{k}'pq} \left(\frac{\partial U_{\mathbf{k}'}}{\partial X_{\mathbf{k}'pq}} v_{\mathbf{k}'pq}^X + \frac{\partial U_{\mathbf{k}'}}{\partial Y_{\mathbf{k}'pq}} v_{\mathbf{k}'pq}^Y \right) \right]_{ii}, \\ \Sigma_{\mathbf{k}mn}^Y &= -p \sum_{\mathbf{T}A,i} Q_{\mathbf{T}A,\mathbf{0}i}^{p-1} \Re \left[\frac{\partial U_{\mathbf{k}}^\dagger}{\partial Y_{\mathbf{k}mn}} P_{\mathbf{T}A,\mathbf{kk}'} \sum_{\mathbf{k}'pq} \left(\frac{\partial U_{\mathbf{k}'}}{\partial X_{\mathbf{k}'pq}} v_{\mathbf{k}'pq}^X + \frac{\partial U_{\mathbf{k}'}}{\partial Y_{\mathbf{k}'pq}} v_{\mathbf{k}'pq}^Y \right) \right]_{ii},\end{aligned}\quad (17)$$

where the term in the parenthesis can be simplified to

$$\sum_{\mathbf{k}'pq} \frac{\partial U_{\mathbf{k}'}}{\partial X_{\mathbf{k}'pq}} v_{\mathbf{k}'pq}^X + \frac{\partial U_{\mathbf{k}'}}{\partial Y_{\mathbf{k}'pq}} v_{\mathbf{k}'pq}^Y = 2 \sum_{\mathbf{k}'pq} E_{pq} v_{\mathbf{k}'pq} \quad (18)$$

Combining this with the gradient of U [eq. (1)] gives

$$\begin{aligned}\Sigma_{\mathbf{k}} &= \tilde{\Sigma}_{\mathbf{k}} - \tilde{\Sigma}_{\mathbf{k}}^\dagger, \\ \tilde{\Sigma}_{\mathbf{k}mn} &= -2p \sum_{\mathbf{T}A} Q_{\mathbf{T}A,\mathbf{0}n}^{p-1} \sum_{\mathbf{k}'} \left(P_{\mathbf{T}A,\mathbf{kk}'v_{\mathbf{k}'}} \right)_{mn}\end{aligned}\quad (19)$$

3. Connected asymmetric term

$$\begin{aligned}\Sigma_{\mathbf{k}mn}^X &= -\frac{1}{2}p \sum_{\mathbf{T}A,i} Q_{\mathbf{T}A,\mathbf{0}i}^{p-1} \Re \left[P_{\mathbf{T}A,\mathbf{0k}} \left\{ \frac{\partial U_{\mathbf{k}}}{\partial X_{\mathbf{k}mn}}, \sum_{pq} \frac{\partial U_{\mathbf{k}}}{\partial X_{\mathbf{k}pq}} v_{\mathbf{k}pq}^X + \frac{\partial U_{\mathbf{k}}}{\partial Y_{\mathbf{k}pq}} v_{\mathbf{k}pq}^Y \right\} \right]_{ii} \\ \Sigma_{\mathbf{k}mn}^Y &= -\frac{1}{2}p \sum_{\mathbf{T}A,i} Q_{\mathbf{T}A,\mathbf{0}i}^{p-1} \Re \left[P_{\mathbf{T}A,\mathbf{0k}} \left\{ \frac{\partial U_{\mathbf{k}}}{\partial Y_{\mathbf{k}mn}}, \sum_{pq} \frac{\partial U_{\mathbf{k}}}{\partial X_{\mathbf{k}pq}} v_{\mathbf{k}pq}^X + \frac{\partial U_{\mathbf{k}}}{\partial Y_{\mathbf{k}pq}} v_{\mathbf{k}pq}^Y \right\} \right]_{ii}\end{aligned}\quad (20)$$

Using eq. (18) to simplify terms in the parenthesis leads to

$$\begin{aligned}\Sigma_{\mathbf{k}mn}^X &= -p \sum_{\mathbf{T}A,i} Q_{\mathbf{T}A,\mathbf{0}i}^{p-1} \Re \left[P_{\mathbf{T}A,\mathbf{0k}} \left\{ \frac{\partial U_{\mathbf{k}}}{\partial X_{\mathbf{k}mn}}, \sum_{pq} E_{pq} v_{\mathbf{k}pq} \right\} \right]_{ii} \\ \Sigma_{\mathbf{k}mn}^Y &= -p \sum_{\mathbf{T}A,i} Q_{\mathbf{T}A,\mathbf{0}i}^{p-1} \Re \left[P_{\mathbf{T}A,\mathbf{0k}} \left\{ \frac{\partial U_{\mathbf{k}}}{\partial Y_{\mathbf{k}mn}}, \sum_{pq} E_{pq} v_{\mathbf{k}pq} \right\} \right]_{ii}\end{aligned}\quad (21)$$

Using eq. (1) to further simplify the expression leads to

$$\begin{aligned}\Sigma_{\mathbf{k}} &= \tilde{\Sigma}_{\mathbf{k}} - \tilde{\Sigma}_{\mathbf{k}}^\dagger, \\ \tilde{\Sigma}_{\mathbf{k}mn} &= p \sum_i v_{\mathbf{k}mi} \left[\sum_{\mathbf{T}A} Q_{\mathbf{T}A,\mathbf{0}i}^{p-1} (P_{\mathbf{T}A,\mathbf{0k}})_{in} \right] + p \sum_{\mathbf{T}A} Q_{\mathbf{T}A,\mathbf{0}m}^{p-1} (P_{\mathbf{T}A,\mathbf{0k}} v_{\mathbf{k}})_{mn}\end{aligned}\quad (22)$$

Finally, using $P_{\mathbf{T}A,\mathbf{k}0} = P_{\mathbf{T}A,\mathbf{0k}}^\dagger$, one can convert eqs. (16), (19) and (22) to Eqn M24–26 in the main text.

F. Hessian diagonal

The Hessian diagonal is defined as:

$$\begin{aligned} D_{\mathbf{k}mn}^X &= \frac{\partial^2 L}{\partial X_{\mathbf{k}mn}^2} = \tilde{D}_{\mathbf{k}}^X + \tilde{D}_{\mathbf{k}}^{X\top} \\ D_{\mathbf{k}mn}^Y &= \frac{\partial^2 L}{\partial Y_{\mathbf{k}mn}^2} = \tilde{D}_{\mathbf{k}}^Y + \tilde{D}_{\mathbf{k}}^{Y\top} \end{aligned} \quad (23)$$

where the second equality explicitly shows its symmetric nature.

1. Disconnected term

$$\begin{aligned} D_{\mathbf{k}mn}^X &= -p(p-1) \sum_{\mathbf{T}_{A,i}} Q_{\mathbf{T}_{A,0i}}^{p-2} \left(\frac{\partial Q_{\mathbf{T}_{A,0i}}}{\partial X_{\mathbf{k}mn}} \right)^2 \\ &= -4p(p-1) \sum_{\mathbf{T}_{A,i}} Q_{\mathbf{T}_{A,0i}}^{p-2} [\Re(P_{\mathbf{T}_{A,0k}})_{mn}]^2 \delta_{mi} + (m \leftrightarrow n) \\ &= -4p(p-1) \sum_{\mathbf{T}_A} Q_{\mathbf{T}_{A,0m}}^{p-2} [\Re(P_{\mathbf{T}_{A,0k}})_{mn}]^2 + (m \leftrightarrow n) \end{aligned} \quad (24)$$

$$\begin{aligned} D_{\mathbf{k}mn}^Y &= -p(p-1) \sum_{\mathbf{T}_{A,i}} Q_{\mathbf{T}_{A,0i}}^{p-2} \left(\frac{\partial Q_{\mathbf{T}_{A,0i}}}{\partial Y_{\mathbf{k}mn}} \right)^2 \\ &= -4p(p-1) \sum_{\mathbf{T}_{A,i}} Q_{\mathbf{T}_{A,0i}}^{p-2} [\Im(P_{\mathbf{T}_{A,0k}})_{mn}]^2 \delta_{mi} + (m \leftrightarrow n) \\ &= -4p(p-1) \sum_{\mathbf{T}_A} Q_{\mathbf{T}_{A,0m}}^{p-2} [\Im(P_{\mathbf{T}_{A,0k}})_{mn}]^2 + (m \leftrightarrow n) \end{aligned} \quad (25)$$

$$\begin{aligned} \tilde{D}_{mn}^X &= -4p(p-1) \sum_{\mathbf{T}_A} Q_{\mathbf{T}_{A,0m}}^{p-2} [(\Re P_{\mathbf{T}_{A,0k}})_{mn}]^2 \\ \tilde{D}_{mn}^Y &= -4p(p-1) \sum_{\mathbf{T}_A} Q_{\mathbf{T}_{A,0m}}^{p-2} [(\Im P_{\mathbf{T}_{A,0k}})_{mn}]^2 \end{aligned} \quad (26)$$

2. Connected asymmetric term

$$\begin{aligned}
D_{\mathbf{k}mn}^X &= -2p \sum_{\mathbf{T}A,i} Q_{\mathbf{T}A,\mathbf{0}i}^{p-1} \Re \left(P_{\mathbf{T}A,\mathbf{0}k} \frac{\partial^2 U_{\mathbf{k}}}{\partial X_{\mathbf{k}mn}^2} \right)_{ii} \\
&= -2p \sum_{\mathbf{T}A,i} Q_{\mathbf{T}A,\mathbf{0}i}^{p-1} \Re \left[P_{\mathbf{T}A,\mathbf{0}k} (E_{mn} - E_{nm})^2 \right]_{ii} \\
&= 2p \sum_{\mathbf{T}A,i} Q_{\mathbf{T}A,\mathbf{0}i}^{p-1} \Re \left(P_{\mathbf{T}A,\mathbf{0}k} E_{mm} \right)_{ii} + (m \leftrightarrow n)
\end{aligned} \tag{27}$$

$$\begin{aligned}
D_{\mathbf{k}mn}^Y &= -2p \sum_{\mathbf{T}A,i} Q_{\mathbf{T}A,\mathbf{0}i}^{p-1} \Re \left(P_{\mathbf{T}A,\mathbf{0}k} \frac{\partial^2 U_{\mathbf{k}}}{\partial Y_{\mathbf{k}mn}^2} \right)_{ii} \\
&= 2p \sum_{\mathbf{T}A,i} Q_{\mathbf{T}A,\mathbf{0}i}^{p-1} \Re \left[P_{\mathbf{T}A,\mathbf{0}k} (E_{mn} + E_{nm})^2 \right]_{ii} \\
&= 2p \sum_{\mathbf{T}A,i} Q_{\mathbf{T}A,\mathbf{0}i}^{p-1} \Re \left(P_{\mathbf{T}A,\mathbf{0}k} E_{mm} \right)_{ii} + (m \leftrightarrow n)
\end{aligned} \tag{28}$$

Therefore

$$\boxed{\tilde{D}_{\mathbf{k}mn}^X = \tilde{D}_{\mathbf{k}mn}^Y = 2p \sum_{\mathbf{T}A} Q_{\mathbf{T}A,\mathbf{0}m}^{p-1} (\Re P_{\mathbf{T}A,\mathbf{0}k})_{mm}} \tag{29}$$

3. Connected symmetric term

$$\begin{aligned}
D_{\mathbf{k}mn}^X &= -2p \sum_{\mathbf{T}A,i} Q_{\mathbf{T}A,\mathbf{0}i}^{p-1} \Re \left(\frac{\partial U_{\mathbf{k}}^\dagger}{\partial X_{\mathbf{k}mn}} P_{\mathbf{T}A,\mathbf{kk}} \frac{\partial U_{\mathbf{k}}}{\partial X_{\mathbf{k}mn}} \right)_{ii} \\
&= 2p \sum_{\mathbf{T}A,i} Q_{\mathbf{T}A,\mathbf{0}i}^{p-1} \Re \left[(E_{mn} - E_{nm}) P_{\mathbf{T}A,\mathbf{kk}} (E_{mn} - E_{nm}) \right]_{ii} \\
&= -2p \sum_{\mathbf{T}A,i} Q_{\mathbf{T}A,\mathbf{0}i}^{p-1} \Re \left(E_{mn} P_{\mathbf{T}A,\mathbf{kk}} E_{nm} \right)_{ii} + (m \leftrightarrow n)
\end{aligned} \tag{30}$$

$$\begin{aligned}
D_{\mathbf{k}mn}^Y &= -2p \sum_{\mathbf{T}A,i} Q_{\mathbf{T}A,\mathbf{0}i}^{p-1} \Re \left(\frac{\partial U_{\mathbf{k}}^\dagger}{\partial Y_{\mathbf{k}mn}} P_{\mathbf{T}A,\mathbf{kk}} \frac{\partial U_{\mathbf{k}}}{\partial Y_{\mathbf{k}mn}} \right)_{ii} \\
&= -2p \sum_{\mathbf{T}A,i} Q_{\mathbf{T}A,\mathbf{0}i}^{p-1} \Re \left[(E_{mn} + E_{nm}) P_{\mathbf{T}A,\mathbf{kk}} (E_{mn} + E_{nm}) \right]_{ii} \\
&= -2p \sum_{\mathbf{T}A,i} Q_{\mathbf{T}A,\mathbf{0}i}^{p-1} \Re \left(E_{mn} P_{\mathbf{T}A,\mathbf{kk}} E_{nm} \right)_{ii} + (m \leftrightarrow n)
\end{aligned} \tag{31}$$

Therefore

$$\boxed{\tilde{D}_{\mathbf{k}mn}^X = \tilde{D}_{\mathbf{k}mn}^Y = -2p \sum_{\mathbf{T}A} Q_{\mathbf{T}A,\mathbf{0}m}^{p-1} (\Re P_{\mathbf{T}A,\mathbf{kk}})_{nn}} \tag{32}$$

III. JACOBI SWEEP

A. General consideration

A general real-valued, translationally symmetric Jacobi rotation can be written as

$$\begin{bmatrix} \tilde{w}_{\mathbf{R}_0, i} & \tilde{w}_{\mathbf{R}_0 + \mathbf{R}, j} \end{bmatrix} = \begin{bmatrix} w_{\mathbf{R}_0, i} & w_{\mathbf{R}_0 + \mathbf{R}, j} \end{bmatrix} \begin{bmatrix} \cos \theta & \sin \theta \\ -\sin \theta & \cos \theta \end{bmatrix}, \quad (33)$$

which mixes $w_{\mathbf{0}, i}$ with $w_{\mathbf{R}, j}$ and, by translational covariance, applies the same rotation to all their lattice translates. Fourier transforming eq. (33) yields the corresponding k -space formulation,

$$\begin{bmatrix} \tilde{\phi}_{\mathbf{k}i} & \tilde{\phi}_{\mathbf{k}j} \end{bmatrix} = \begin{bmatrix} \phi_{\mathbf{k}i} & \phi_{\mathbf{k}j} \end{bmatrix} \begin{bmatrix} \cos \theta & e^{i\mathbf{k}\cdot\mathbf{R}} \sin \theta \\ -e^{-i\mathbf{k}\cdot\mathbf{R}} \sin \theta & \cos \theta \end{bmatrix}, \quad (34)$$

which corresponds to a k -dependent 2×2 rotation between Bloch orbitals i and j .

B. Working equations for $p = 2$

To determine the optimal rotation angle θ , consider the PM objective for a pair of WFs $(\mathbf{0}i, \mathbf{R}j)$ after applying the Jacobi rotation in eq. (33):

$$\tilde{L}_{ij} = \sum_{\mathbf{T}A} [(\tilde{P}_{\mathbf{T}A, \mathbf{00}})_{ii}^2 + (\tilde{P}_{\mathbf{T}A, \mathbf{00}})_{jj}^2]. \quad (35)$$

Using

$$\begin{aligned} \tilde{w}_{\mathbf{0}i} &= w_{\mathbf{0}i} \cos \theta - w_{\mathbf{R}j} \sin \theta, \\ \tilde{w}_{\mathbf{0}j} &= w_{-\mathbf{R}i} \sin \theta + w_{\mathbf{0}j} \cos \theta, \end{aligned} \quad (36)$$

the diagonal projection matrix elements after rotation become

$$\begin{aligned} (\tilde{P}_{\mathbf{T}A, \mathbf{00}})_{ii} &= (P_{\mathbf{T}A, \mathbf{00}})_{ii} \cos^2 \theta + (P_{\mathbf{T}A, \mathbf{RR}})_{jj} \sin^2 \theta - 2 \Re(P_{\mathbf{T}A, \mathbf{0R}})_{ij} \cos \theta \sin \theta, \\ (\tilde{P}_{\mathbf{T}A, \mathbf{00}})_{jj} &= (P_{\mathbf{T}A, (-\mathbf{R})(-\mathbf{R})})_{ii} \sin^2 \theta + (P_{\mathbf{T}A, \mathbf{00}})_{jj} \cos^2 \theta + 2 \Re(P_{\mathbf{T}A, (-\mathbf{R})\mathbf{0}})_{ij} \cos \theta \sin \theta \\ &= (P_{\mathbf{T}A, \mathbf{00}})_{ii} \sin^2 \theta + (P_{\mathbf{T}A, \mathbf{RR}})_{jj} \cos^2 \theta + 2 \Re(P_{\mathbf{T}A, \mathbf{0R}})_{ij} \cos \theta \sin \theta. \end{aligned} \quad (37)$$

In the second line for $(\tilde{P}_{\mathbf{T}A, \mathbf{00}})_{jj}$, we have used translational symmetry together with the fact that \mathbf{T} is summed over in the final objective. The change in the PM objective due to the $(\mathbf{0}i, \mathbf{R}j)$ rotation is therefore

$$\Delta L_{ij}(\theta) = \tilde{L}_{ij}(\theta) - L_{ij} = -\frac{1}{2} \sin 2\theta [(A_{\mathbf{0R}})_{ij} \cos 2\theta + (B_{\mathbf{0R}})_{ij} \sin 2\theta], \quad (38)$$

where we have introduced the intermediates

$$\begin{aligned}(A_{\mathbf{0R}})_{ij} &= 4 \sum_{\mathbf{T}_A} [(P_{\mathbf{T}_A, \mathbf{00}})_{ii} - (P_{\mathbf{T}_A, \mathbf{RR}})_{jj}] \Re(P_{\mathbf{T}_A, \mathbf{0R}})_{ij}, \\ (B_{\mathbf{0R}})_{ij} &= \sum_{\mathbf{T}_A} [(P_{\mathbf{T}_A, \mathbf{00}})_{ii} - (P_{\mathbf{T}_A, \mathbf{RR}})_{jj}]^2 - [2 \Re(P_{\mathbf{T}_A, \mathbf{0R}})_{ij}]^2.\end{aligned}\tag{39}$$

Setting $\Delta L'_{ij}(\theta) = 0$ yields

$$\tan 4\theta = -\frac{(A_{\mathbf{0R}})_{ij}}{(B_{\mathbf{0R}})_{ij}}.\tag{40}$$

Equation (40) can be interpreted as follows:

1. Since the input orbitals are already at a stationary point of the PM functional, $\theta = 0$ is a trivial solution of eq. (40), implying that the right-hand side vanishes. The non-trivial solutions therefore satisfy $\tan 4\theta = 0$, i.e., $4\theta = n\pi$ with $n \neq 0$.
2. Furthermore, it is sufficient to restrict θ to the interval $[0, \pi)$, because a rotation by $\theta = \pi$ corresponds to a simultaneous sign change of the two orbitals, which leaves the PM objective invariant, and any $\theta > \pi$ can be mapped back into $[0, \pi)$.

We therefore conclude that the only distinct non-trivial solutions are

$$\theta = \frac{\pi}{4}, \frac{\pi}{2}, \frac{3\pi}{4}.\tag{41}$$

In practice, we can calculate ΔL_{ij} for all possible θ values in eq. (41) to find one that maximizes the PM objective.

C. Extension for $p > 2$

The derivation above strictly assumes $p = 2$. A similar derivation for $p = 3$ leads to the same condition eq. (40) for determining θ except that the two intermediates are defined as

$$\begin{aligned}(A_{\mathbf{0R}})_{ij} &= 4 \sum_{\mathbf{T}_A} [(P_{\mathbf{T}_A, \mathbf{0R}})_{ii}^2 - (P_{\mathbf{T}_A, \mathbf{0R}})_{jj}^2] \Re(P_{\mathbf{T}_A, \mathbf{0R}})_{ij}, \\ (B_{\mathbf{0R}})_{ij} &= \sum_{\mathbf{T}_A} [(P_{\mathbf{T}_A, \mathbf{0R}})_{ii} + (P_{\mathbf{T}_A, \mathbf{0R}})_{jj}] \left\{ [(P_{\mathbf{T}_A, \mathbf{0R}})_{ii} - (P_{\mathbf{T}_A, \mathbf{0R}})_{jj}]^2 - [2 \Re(P_{\mathbf{T}_A, \mathbf{0R}})_{ij}]^2 \right\},\end{aligned}\tag{42}$$

For general $p > 3$, an analytic derivation becomes cumbersome. However, the second argument above (periodicity in θ) always holds, and we have numerically validated that the first argument holds for $p \leq 6$ (which arguably already covers most use cases of PM localization). We therefore *postulate* that the first argument remains valid for all $p \geq 2$.

D. Efficient implementation and computational cost

In practice, we evaluate $\Delta L_{ij}(\theta)$ numerically for the three candidate angles in eq. (41) and check whether any of them increases the PM objective. The computational cost of this Jacobi stability check scales as

$$O(N_k^2 n_{\text{proj}} n_{\text{orb}}^2) \quad (43)$$

for building the $(P_{TA,kR})_{ij}$ intermediate. This cost is modest and comparable to that of a single gradient evaluation.

However, one can reasonably expect that pairwise instabilities primarily involve orbital pairs that are not too far apart in real space. We therefore can optionally restrict the real-space shifts in eq. (34) to satisfy

$$|\mathbf{R}| < R_{\max}, \quad (44)$$

for a chosen cutoff R_{\max} , which provides a controllable reduction in computational cost. Let N_R denote the number of lattice vectors \mathbf{R} satisfying eq. (44). Under this restriction, the cost of the Jacobi stability check becomes

$$O(N_k N_R n_{\text{proj}} n_{\text{orb}}^2), \quad (45)$$

which is linear in N_k when N_R is independent of N_k . We choose $R_{\max} = 10$ Bohr in this work, which covers WF pairs that are separated by roughly 5 chemical bonds.